Towards Quantitative Measurements of Tissue Microstructure using Temporal Diffusion Spectroscopy

By

Hua Li

Dissertation
Submitted to the Faculty of the
Graduate School of Vanderbilt University
in partial fulfillment of the requirements
for the degree of

DOCTOR OF PHILOSOPHY
in

Physics
August, 2015
Nashville, Tennessee

Approved:
John C. Gore
Junzhong Xu
Adam W. Anderson
Mark D. Does
Daniel F. Gochberg

ACKNOWLEDGEMENTS

I would like to express my deepest appreciation to my advisor Dr. John Gore, who has the altitude to see the big picture and the depth to perceive the essential nature: he is the best of the best. Without his persistent guidance and support, this dissertation would never have been possible. I would like to give my great thank to my friend, my partner, my co-mentor Dr. Junzhong Xu, who taught me how to be a research scientist step by step.

I would also like to thank Dr. Adam Anderson, Dr. Mark Does, Dr. Daniel Gochberg, Dr. Chad Quarles for being my committee members and for providing significant insight to my studies. I am also grateful to my colleagues Zhongliang Zu, Jingping Xie, Xiaoyu Jiang, Zou Yue, Feng Wang for numerous help. I am so lucky to join VUIIS.

Finally, I would like to thank my family for everything. Thank my wife Fang for waiting for me to come home.

TABLE OF CONTENTS

LIST OF FIGURES

CHAPTER I

CHAPTER II

CHAPTER III

CHAPTER IV

CHAPTER V

LIST OF TABLES

CHAPTER IV

CHAPTER V

CHAPTER I
INTRODUCTION

Brief history of NMR

Nuclear magnetic resonance (NMR) is a physical phenomenon in which nuclei in a magnetic field absorb and re-emit energy at a specific resonance frequency. It is a way to exploit the molecular properties of materials non-invasively via applying magnetic field and electromagnetic radiation simultaneously. Since its discovery, NMR has been widely adapted and applied to various fields, including biology, chemistry, physics, medicine, food science and the petroleum industry. A brief look at the NMR related Nobel Prizes reveals the discovery, development, and applications of NMR spectroscopy. In 1922, the German physicists Otto Stern and Walther Gerlach conducted the famous Stern-Gerlach experiment (1), from which the existence of spin quantization was inferred. The concept of spin was then proposed and gradually understood in the 1920s. In 1933, Otto Stern discovered the magnetic moment of the proton and thus confirmed that the proton exhibits spin as well (2). The Nobel Prize in Physics 1943 was awarded to Otto Stern for this discovery.

Using an extended version of the Stern-Gerlach apparatus, Isidor Isaac Rabi and colleagues developed a molecular beam resonance method for measuring nuclear magnetic moments (3,4). It was demonstrated that the magnetic spin states of nuclei could be switched from one state to the other using a varying magnetic field. They also discovered that the state transitions could be realized by varying the frequency of radiofrequency fields. The Nobel Prize in Physics 1944 was awarded to Rabi for his resonance method for recording the magnetic properties of atomic nuclei.

The Nobel Prize in Physics 1952 was awarded jointly to Felix Bloch and Edward Mills Purcell for their development of new methods for nuclear magnetic resonance measurements. Quite different from the molecular beam resonance method, Bloch and Purcell independently observed the resonance phenomena in condensed materials containing protons. Although the same phenomena were involved, their experiments were much different. Purcell and colleagues had been able to observe the absorption of radiofrequency energy caused by the state transitions (5), while Bloch and colleagues

focused on the re-emission of radiofrequency energy induced by the perturbed magnetization (6). These studies laid the foundation for the widespread use of NMR in analytical chemistry.

The Nobel Prize in Chemistry 1991 was awarded to Richard Ernst for his contributions towards the development of Fourier Transform NMR spectroscopy. In the first few decades of NMR spectroscopy, NMR absorption spectra were typically obtained using a fixed magnetic field and varying the RF frequency. This technique is slow since it detects only a narrow region of a spectrum at a time. Ernst introduced pulsed Fourier Transform (FT) NMR spectroscopy to efficiently obtain spectra over a range of frequencies that were inversely proportional to the pulse duration. Thus, the sensitivity of NMR techniques increased dramatically. It should be noted that the time-domain signals must be Fourier transformed in order to obtain the frequency-domain NMR spectra.

The development of FT NMR methods had significant influence on NMR applications. Multi-dimensional FT NMR experiments were widely applied for studying biomolecules. Kurt Wüthrich won the Nobel Prize in Chemistry 2002 for determining the three-dimensional structure of biological macromolecules in solution using NMR spectroscopy. NMR spectroscopy has been developed into an essential tool studying the structure, dynamics, and interactions of biological macromolecules.

Another exciting application of NMR spectroscopy began in 1973 when Paul Lauterbur introduced magnetic field gradients to spatially vary resonance frequencies (7). The NMR frequency could be used as a measure of position along the gradient direction, and further, 2D images could be obtained by repeating the measurement along different gradient directions. Meanwhile, Peter Mansfield developed methods to selectively excite a region within a sample and a theory of MR image formation based on multidimensional Fourier transforms (8). Peter Mansfield also developed echo-planar imaging for fast imaging acquisition (9). The Nobel Prize in Physiology or Medicine 2003 was awarded jointly to them for their discoveries concerning magnetic resonance imaging.

Basic principles of NMR and MRI

In physics, Larmor precession describes the motions of magnetic moments about an external magnetic field. The basic NMR relationship is

$$\omega = \gamma B_0 \qquad [1.1]$$

where ω is the Larmor frequency, γ is the gyromagnetic ratio, and B_0 is the external magnetic field strength. Resonance absorption is expected to occur only when the frequency of applied electromagnetic radiation is equal to the Larmor frequency ω. As an example, the Larmor frequency for protons at 7T is ~ 300 MHz.

In an equilibrium state, the macroscopic nuclear magnetization ($\mathbf{M} = (M_x, M_y, M_z)$) is parallel to the applied external magnetic field. By applying radiofrequency energy, the magnetization can be rotated away from its equilibrium position (M_0). It will then precess about the magnetic field at the Larmor frequency and return to its equilibrium state due to relaxation. Bloch proposed a set of macroscopic equations to describe the time evolution of magnetization (6).

$$\begin{aligned}
\frac{dM_x(t)}{dt} &= \gamma(M(t)\times B(t))_x - \frac{M_x(t)}{T_2} \\
\frac{dM_y(t)}{dt} &= \gamma(M(t)\times B(t))_y - \frac{M_y(t)}{T_2} \\
\frac{dM_z(t)}{dt} &= \gamma(M(t)\times B(t))_z - \frac{M_z(t)-M_0}{T_2}
\end{aligned} \qquad [1.2]$$

T_1 and T_2 are longitudinal and transverse relaxation times, respectively. **B**(t) is the applied magnetic fields including the static magnetic field B_0 and the radiofrequency pulses. The use of a rotating reference frame helps better visualize the magnetization evolution under the action of RF pulses (10). Note that Bloch equations are macroscopic equations. They do not describe the evolution of individual nuclear magnetic moments, which would require a quantum mechanical description.

To obtain MR images, Lauterber proposed to spatially vary resonance frequencies using magnetic field gradients (7). With such a gradient, the Larmor frequency is position dependent and becomes

$$\omega(x) = \gamma(B_0 + Gx) \qquad [1.3]$$

where G is the gradient amplitude in direction *x*. Recall that the time-domain signal is the Fourier transform of the frequency-domain NMR spectrum. The measured signal (s(t))

could further be converted to the spin density of the sample (ρ(x)) along direction *x* via Eq. [1.3]. Mathematically, the accumulated phase due to the applied gradient is

$$\phi_G(x,t) = -\gamma x \int_0^t dt' G(t') \qquad [1.4]$$

The signal in reference frame rotating at $\omega_0 = \gamma B_0$ is given by

$$s(t) = \int dx \rho(x) e^{i\phi_G(x,t)} \qquad [1.5]$$

This can be rewritten as

$$s(k) = \int dx \rho(x) e^{-i2\pi kx} \qquad [1.6]$$

where the spatial frequency *k* is a function of time and gradient.

$$k(t) = \frac{\gamma}{2\pi} \int_0^t dt' G(t') \qquad [1.7]$$

Eq. [1.6] shows that the signal *s*(*k*) is the Fourier transform of the spin density of the sample along gradient direction *x*. The spin density is therefore the inverse Fourier transform of the singal:

$$\rho(x) = \int s(k) e^{i2\pi kx} \, dk \qquad [1.8]$$

This Fourier relationship between signal and spin density is a basic relationship that can be extended to 2 and 3 dimensions and forms the basis for MR image acquisition and reconstruction.

Basic principles of Diffusion MRI

Diffusion is the random translational (or Brownian) motion of molecules or ions that is driven by internal thermal energy. Fick devised two differential equations to quantitatively describe diffusion of molecules under a net flux over a concentration gradient (11).

$$\begin{aligned} \boldsymbol{J}(\boldsymbol{r},t) &= -D\nabla c(\boldsymbol{r},t) \\ \frac{\partial c(\boldsymbol{r},t)}{\partial t} &= D\nabla^2 c(\boldsymbol{r},t) \end{aligned} \qquad [1.9]$$

where $\boldsymbol{J}$ is the flux of particles at spatial position $\boldsymbol{r}$ and time *t*, *D* is the diffusion coefficient and c($\boldsymbol{r}$,*t*) is the concentration of particles. To describe self-diffusion in the absence of internal concentration gradients, such as molecular motions in pure water, it is

possible to use Fick's second law of diffusion with c($\boldsymbol{r}$,t) replaced by a probability function P($\boldsymbol{r}_0|\boldsymbol{r}$,$t$) which gives the probability of a particle having moved from position $\boldsymbol{r}_0$ to position $\boldsymbol{r}$ over time t.

$$\frac{\partial \mathrm{P}(\boldsymbol{r}_0|\boldsymbol{r},t)}{\partial t} = D\nabla^2 \mathrm{P}(\boldsymbol{r}_0|\boldsymbol{r},t) \qquad [1.10]$$

The solution for free diffusion is:

$$\mathrm{P}(r_0|r,t) = (4\pi Dt)^{-1/2} \exp[-(r-r_0)^2 / 4Dt] \qquad [1.11]$$

which has a Gaussian dependence on the displacement. For the study of diffusion in biological systems, the free movements of water molecules may be hindered or restricted by a wide range of factors like the presence of cellular membranes, high concentrations of proteins and binding to macromolecules. The displacement probability is then not well represented by a simple Gaussian distribution, but the deviations from Gaussian distribution may provide useful information about the geometrical constraints and tissue microstructure.

Diffusion measurements by NMR rely on detecting the signal loses caused by diffusion dependent phase dispersal in an applied gradient field. The study of diffusion using NMR goes back to 1950 when Erwin Hahn first described the effects of self-diffusion on spin-echo signal (12). Herman Carr and Edward Purcell extended Hahn's analysis and quantified the molecular self-diffusion coefficient of water via measuring the transverse relaxation time under a constant magnetic field gradient (13). Torry extended the Bloch equations by the addition of diffusion terms (14), based on which, Stejskal and Tanner further studied the effect of a time-dependent magnetic field gradient on the spin-echo experiment and developed the pulsed gradient spin-echo (PGSE) method to directly measure the molecular diffusion rate (15). The conventional PGSE sequence is shown in Figure 1.1. A $\pi/2$ excitation pulse rotates the magnetization from the longitudinal direction to the transverse plane, after which all the spins have the same initial phase and are phase coherent. A first magnetic field gradient (magnitude G) causes a position-dependent frequency change $\Delta\omega = \gamma G r_1$ where r_1 is the current spin position. Assuming the gradient duration δ is short, the spins acquire a position-dependent phase $\phi_1 = \gamma\delta G r_1$ at the end of the first gradient. The π refocusing pulse functions to reverse the phase, after which a second gradient leads to another phase change $\phi_2 = -\gamma\delta G r_2$ where r_2

is the spin position when the second magnetic gradient field is on. If all spins are stationary, $r_1 = r_2$ such that all spins have zero phase ($(\phi_1 + \phi_2) = 0$) at the time of data acquisition.

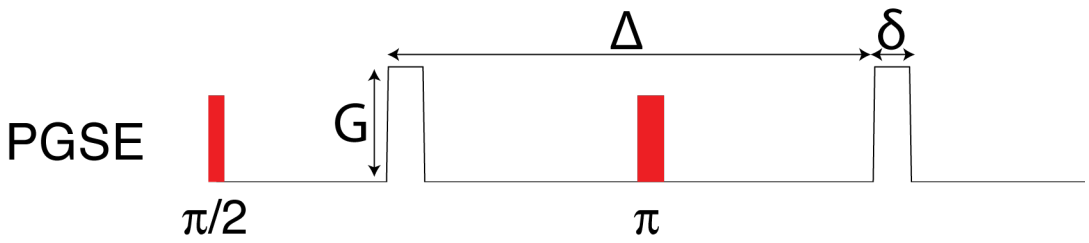

Figure 1.1 Conventional PGSE sequence. The pulse sequence can be sensitized for diffusion by the application of a pair of pulsed magnetic field gradients surrounding the π pulse with gradient amplitude G, duration δ and separation Δ.

However, if spins change spatial positions during the separation Δ, the phase induced by the second gradient no longer cancels the phase induced by the first gradient ($(\phi_1 + \phi_2) \neq 0$). Therefore, application of magnetic field gradients in the presence of diffusion leads to phase dispersal across the sample, which in turn leads to phase cancellation and hence signal loss when signal is acquired from the entire sample.

The Bloch-Torry equations can be used to describe the precessing magnetization mathematically. The precessing magnetization ($\Psi(r,t)$) unaffected by relaxation can be described by

$$\frac{\partial \Psi(r,t)}{\partial t} = -i\gamma r G(t)\Psi + \nabla \bullet D\nabla\Psi \qquad [1.12]$$

The solution is

$$\Psi(r,t) = M_0 \exp(-bD - irF(t)) \qquad [1.13]$$

where

$$F(t) = \gamma \int_0^t G(t')dt'$$
$$b(t) = \gamma \int_0^t |F(t')|^2 \, dt' \qquad [1.14]$$

For free diffusion measured with the PGSE sequence, the signal would be an exponential decay:

$$S = S_0 e^{-bD} \qquad [1.15]$$

where the diffusion weighting factor b is

$$b = \gamma^2 \delta^2 G^2 (\Delta - \delta / 3) \qquad [1.16]$$

The effective diffusion time is usually defined as $\Delta_{eff} = \Delta - \delta / 3$.

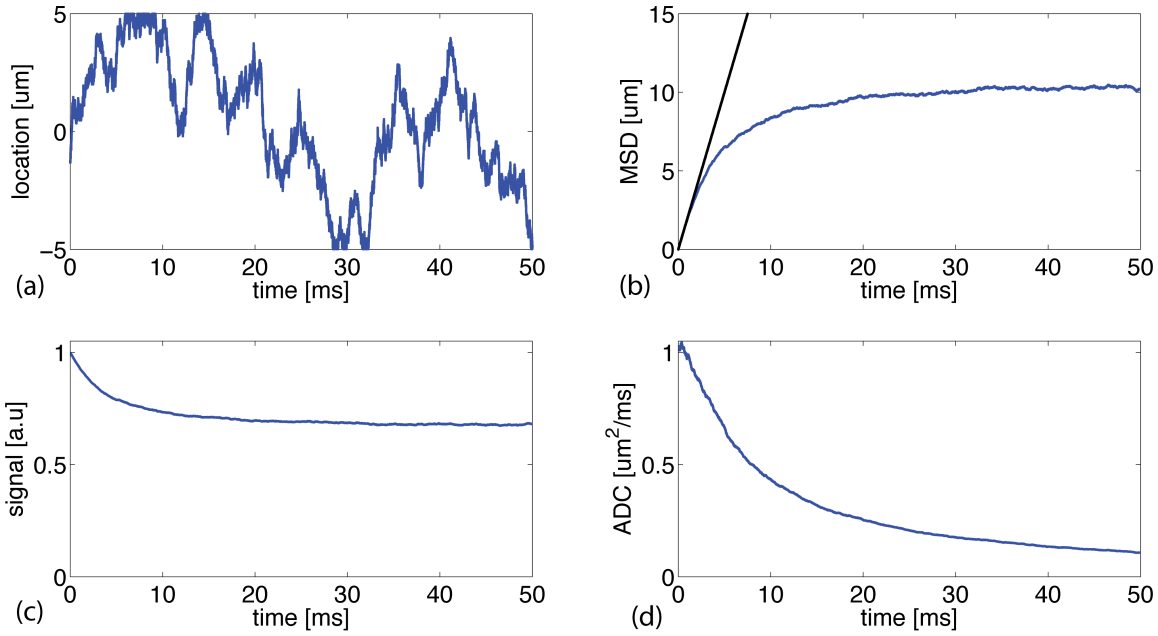

Figure 1.2 The simulated results for 1D restricted diffusion between two impermeable planes. The position of a typical particle is shown in (a). The mean square displacement (blue curve) is shown in (b). The black line in (b) represents the expected mean square displacement based on Einstein relation. The simulated signal and ADC for PGSE measurement are shown in (c) and (d), respectively.

Figure 1.2 shows the simulated results for diffusion between two impermeable planes separated by a distance of 10 μm with the intrinsic diffusion coefficient D = 1 $\mu m^2/ms$. Figure 1.2 (a) shows the location of a typical particle. The blue curve in Figure 1.2 (b) shows the values of mean square displacement. The black line represents the expected MSD for free diffusion with the same diffusion rate based on the Einstein relation. Figure 1.2 (c) shows the simulated signal for PGSE measurement with constant

gradient strength, and Figure 1.2 (d) shows the simulated ADC. In a system with restricting barriers, at extremely short diffusion times (when most spins have not moved to the barrier), water diffusion appears Gaussian and the mean square displacement of molecules along a gradient direction increases in proportion to t as predicted by the Einstein relation $< L >^2 = 2Dt$ where <L> is the root mean square displacement. When the distance moved in the diffusion time is comparable with the sizes and spaces of structures, the measured apparent diffusion coefficient (ADC) decreases and reflects the dimensions of such barriers. At extremely long diffusion times (when all diffusing spins have encountered boundaries many times), the measured ADC is asymptotic and does not distinguish different sizes of restrictions. Thus, to measure barrier sizes or be sensitive to structures below this scale, it is necessary to make the diffusion time short enough. However, due to gradient hardware limitations, the shortest diffusion times practical using typical MRI scanners are about 10-20 ms. The corresponding one-dimensional root mean square displacements (RMSDs) of diffusion molecules are then on the order of 10 μm (assuming D = 3 $\mu m^2/ms$), which limits the information obtainable on sizes smaller than this, which is typical of cell dimensions in biological tissues.

Basic principles of Temporal Diffusion Spectroscopy

The Bloch-Torrey equations are phenomenological equations. This approach could help understand the signal decay in a simple way but it does not connect the signals with structure properties directly. Using a density matrix calculation, Stepisnik analyzed the self-diffusion measurements under gradients with more general shapes (16,17). The results showed that the NMR response can be related to the spectrum of the single-particle velocity autocorrelation function (<$\boldsymbol{v}(t_1)\boldsymbol{v}(t_2)$>), the shape of which then contains information about the structure of the medium. Briefly, the attenuated signal due to the diffusion gradient **g**(t) can be expressed as

$$S = S_0 \exp\left\{-\frac{1}{2}\int_0^\infty \int_0^\infty \boldsymbol{F}(t_1) < \boldsymbol{v}(t_1)\boldsymbol{v}(t_2) > \boldsymbol{F}(t_2)\, dt_1\, dt_2\right\} \qquad [1.17]$$

where $\boldsymbol{F}(t)$ is the time integral of diffusion gradient

$$\boldsymbol{F}(t) = \gamma \int_0^t \boldsymbol{g}(t')\, dt' \qquad [1.18]$$

The Fourier transform of the velocity autocorrelation function is then the temporal diffusion spectrum $\boldsymbol{D}(\omega)$ where

$$\boldsymbol{D}(\omega) = \frac{1}{2}\int_0^\infty < \boldsymbol{v}(t)\boldsymbol{v}(0) > \exp(-i\omega t)dt \qquad [1.19]$$

Hence, Eq[1.17] becomes

$$S = S_0 \exp(-\frac{1}{\pi}\int_0^\infty \boldsymbol{F}(\omega)\boldsymbol{D}(\omega)\boldsymbol{F}(-\omega)d\omega \qquad [1.20]$$

where the spectrum of the time integral of diffusion gradient is

$$\boldsymbol{F}(\omega) = \int_0^\infty dt \exp(-i\omega t)\boldsymbol{F}(t) = \int_0^\infty dt \exp(-i\omega t)\int_0^t dt' \gamma \boldsymbol{g}(t') \qquad [1.21]$$

It is evident that the attenuated signal is dependent on the diffusion spectrum and gradient waveforms. $\boldsymbol{F}(\omega)$ can be considered as a spectral sampling window. Using appropriately designed gradient waveforms, the diffusion spectrum $\boldsymbol{D}(\omega)$ may be sampled at well-defined single frequencies, and by varying the sampling frequencies, an apparent diffusion spectrum can be obtained (18).

Figure 1.3 shows three typical diffusion gradient waveforms and their corresponding sampling spectra. It is evident that the conventional PGSE method detects mainly the zero-frequency component. The sine-modulated oscillating gradient spin echo method (sin-OGSE) samples the diffusion spectrum at the applied oscillating frequency and zero-frequency components. The cosine-modulated OGSE (cos-OGSE) method probes a narrow range of frequencies centered at the applied oscillating frequency, so, it is more suitable for sampling the apparent diffusion spectrum.

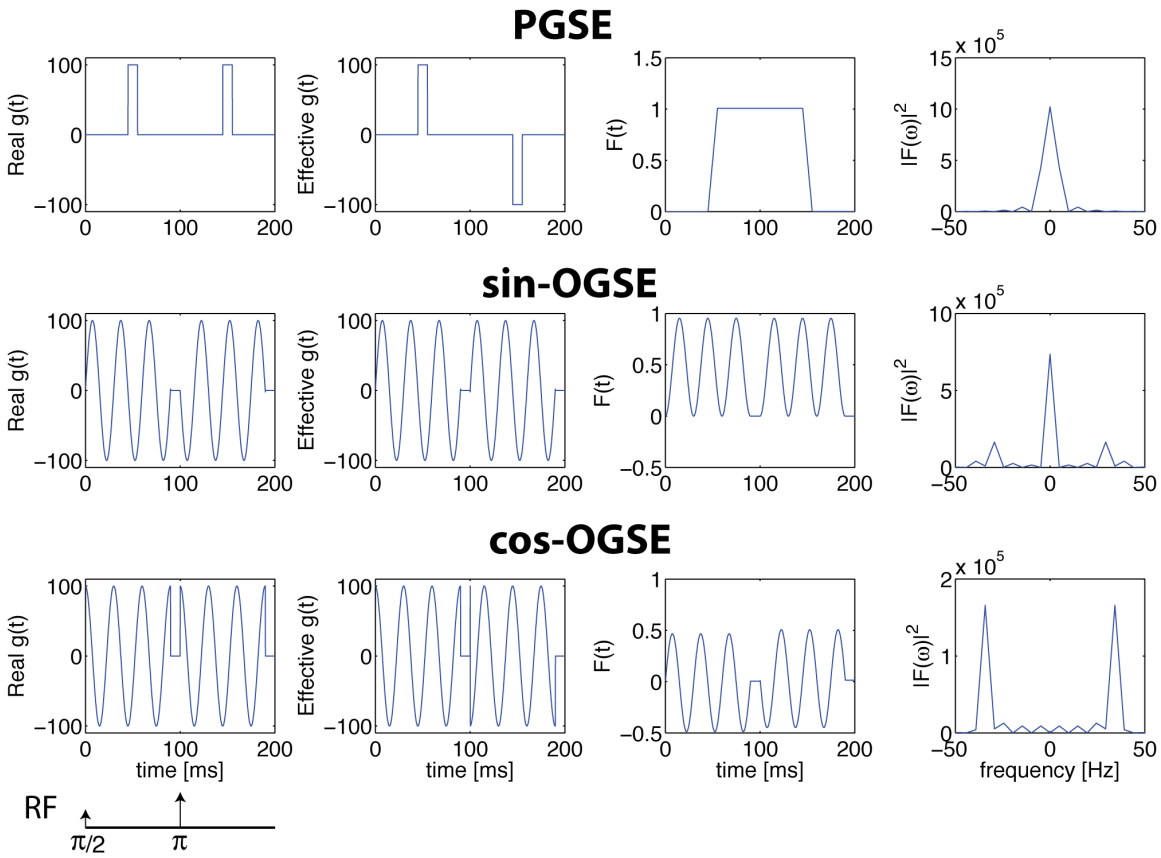

Figure 1.3 Three typical diffusion gradient waveforms and their corresponding sampling spectra.

Similar to the PGSE method, the diffusion weighting factor b can be calculated from Eq. [1.14]. For the sin-OGSE method shown in Figure 1.2, the calculated b-value is

$$b_{\sin} = \frac{3\gamma^2 G^2 \sigma}{4\pi^2 f^2} \qquad [1.22]$$

where σ is the duration of each gradient pulse, and f is the oscillating frequency. For the cos-OGSE method, the result is

$$b_{\cos} = \frac{\gamma^2 G^2 \sigma}{4\pi^2 f^2} \qquad [1.23]$$

The concept of diffusion time is not explicitly defined when the gradient is not a narrow pulse. Based on the equivalence of b-values between PGSE and OGSE sequences, an effective diffusion time for a cosine-modulated OGSE sequence is:

$$\Delta_{\text{eff}} = \frac{1}{4f} \qquad [1.24]$$

It is worth noting that the measured ADC values are unlikely to be the same for PGSE and OGSE measurements with the same effective diffusion time. Figure 1.4 (a) shows the simulated ADC values at different effective diffusion times for water diffusing inside an impermeable sphere with radius = 5 μm. Figure 1.4 (b) shows the simulated ADC values at Δ_{eff} = 5 ms for water diffusing inside an impermeable sphere of different radii. With the same effective diffusion time, the PGSE and cos-OGSE methods usually lead to different ADC values.

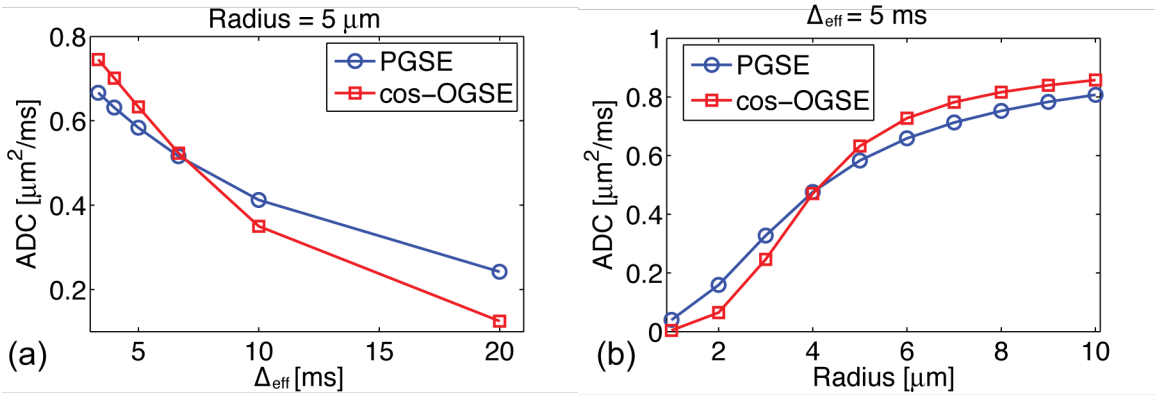

Figure 1.4 Comparison of ADC values measured with PGSE and cos-OGSE methods under the same effective diffusion time. Figure 3(a) shows the case of fixed sphere radius and varied Δ_{eff}. Figure 3(b) shows the ADC values for different radii with Δ_{eff} = 5 ms.

Organization of this Dissertation

OGSE MRI has previously been used to demonstrate how diffusion spectra change in various biological tissues, such as tumor (19) and stroke (20). Diffusion measurements at different frequencies (diffusion times) may be sensitive to structures of different scales and the measured ADCs at high frequencies may better detect intra-cellular microstructural variations (21-24). It has also been successfully implemented for earlier detection of tumor treatment response (25). Besides the information provided by single ADC measurements, the manner in which ADC disperses with gradient frequency (or diffusion time) provides information on the characteristic dimensions of structures within a medium. For example, the dispersion of ADC with oscillating gradient

frequency (Δ_fADC) has been shown to correlate with axon sizes in white matter (26) and provide novel tissue contrast in images of mouse hippocampus and cerebellum (27,28). However, despite increasing interest in applying frequency-dependent ADC to derive novel information on tissue, the relation between ADC spectra and restricting sizes are not always clear. Meanwhile, to better characterize the tissue microstructure, the direct quantitation of restricting dimensions may be more helpful. To this end, several previous studies have tentatively measured the cell sizes in vitro through OGSE measurements, but with the simplest one-pool mathematical model (24,29,30). In this thesis, we will first study the relation between ADC spectra and restricting dimensions and then move to quantify the restricting dimensions with more realistic models and more optimized diffusion measurements.

In chapter 2, the relation between ADC spectra and restricting dimensions are further elucidated and used to derive novel image contrast related to the sizes of intrinsic microstructures. This is the first contribution of this thesis.

Recently, several PGSE-based diffusion approaches have been proposed to measure axon and/or cell sizes quantitatively (31-33). For simplicity, those approaches usually ignored water exchange between the intra- and extracellular spaces. With shorter effective diffusion times, OGSE may be less affected by permeability changes and thus more suitable for estimating structural sizes with the assumption of negligible water exchange. The influence of cell membrane permeability on MR diffusion measurements is studied in depth in chapter 3. The experimental study of the effects of permeability on OGSE measurements is the second contribution of this thesis.

With shorter effective diffusion times, OGSE may be able to detect small structures with higher sensitivity than PGSE. The sensitivity and performance of OGSE for quantitative measurements of structural sizes is explored in chapters 4-5. Chapter 4 considers the simplest one-pool model where water is allowed to diffuse only within impermeable cylinders. In biological tissues, water can exist in both the intra- and extracellular spaces. As a simple two-pool model, the white matter tracts in rat spinal cord were used to examine the performance of OGSE (34). While the OGSE methods are sensitive to small axons, simulations suggest that OGSE would significantly underestimate the axons with diameters larger than 6 μm. In chapter 5, we combined

OGSE measurements with a single PGSE acquisition at relatively long diffusion time to accurately measure large cell sizes (up to 20 μm). Extending the measured diffusion frequency (diffusion time) ranges is the third contribution of this thesis to the quantitative measurements of tissue microstructure using temporal diffusion spectroscopy.

CHAPTER II

STRUCTURAL INFORMATION REVEALED BY TEMPORAL DIFFUSION SPECTROSCOPY

Abstract

Diffusion MRI provides a non-invasive means to characterize tissue microstructure at varying length scales. Apparent diffusion coefficients (ADCs) of tissue water may be measured at relatively long diffusion times with conventional pulsed gradient spin echo (PGSE) methods, or at much shorter effective diffusion times using oscillating gradient spin echo (OGSE) methods. The manner in which ADC disperses with gradient frequency (or diffusion time) provides information on the characteristic dimensions of structures within the medium. For example, the dispersion of ADC with oscillating gradient frequency (Δ_fADC) has been shown to correlate with axon sizes in white matter and provide novel tissue contrast in images of mouse hippocampus and cerebellum. In this study, the relation between ADC spectra and restricting dimensions are further elucidated and used to derive novel image contrast related to the sizes of intrinsic microstructures.

Introduction

Diffusion MRI provides a non-invasive means to characterize tissue microstructure, and has been widely used to detect stroke and monitor tumor response to therapy (35-38). The apparent diffusion coefficients (ADCs) measured at different diffusion times are believed to reflect the structural hindrances and restrictions to free water movement at varying length scales (18). Conventional pulsed gradient spin echo (PGSE) measurements of ADC in biological tissues usually involve relatively long diffusion times (20-40 ms), so the corresponding one-dimensional root mean square displacements (RMSDs) of diffusion molecules are on the order of 10 μm. The ADC measured with PGSE is thus observed to correlate with cellularity in several types of tumors (36,39,40).

Oscillating gradient spin echo (OGSE) methods have been proposed in order to achieve much shorter diffusion times and hence they are able to differentiate smaller structures with higher sensitivity (20,41). For example, the measured ADCs at high

oscillating frequencies have been shown to convey microstructural variations at sub-cellular scales, which may help detect earlier tumor response to treatment before changes in tissue cellularity (19,23-25). Moreover, by varying the oscillating frequencies, an apparent diffusion spectrum can be obtained (41). The manner in which ADC disperses with oscillating frequency provides information on tissue structure over a range of intrinsic length scales and in general may reflect several tissue properties, but some simple features of such spectra have proven empirically useful (18). For example, the initial rate of change of ADC with frequency at low frequencies has been shown to correlate with axon sizes in white matter (26) and provide novel tissue contrast in images of mouse hippocampus and cerebellum (27,28,42). However, despite increasing interest in applying frequency-dependent ADC to derive novel information on tissue (30,43-45), the interpretations of ADC spectra are not always clear.

Restricted diffusion with generalized time-varying diffusion gradient waveforms has been studied previously (46,47). Specifically for water diffusion inside simple geometries using cosine-modulated waveforms, analytical equations describing ADC as a function of frequency have been derived and validated (47-49). In this study, the theory of water diffusion inside an impermeable cylinder was re-examined with emphasis on the rate of frequency-dependent changes in ADC. From this, a simple relation between the rate and cylinder size can be derived for limited ranges of parameters. Simulations and experiments were further studied to illustrate this relation. This study may help better understand the information revealed by the behavior of ADC with frequency and suggests a novel type of parametric image that depicts structural dimensions.

Methods

Theory

For an OGSE sequence with a pair of cosine-modulated gradients on either side of a refocusing pulse, the diffusion weighting b-value is:

$$b = \frac{\gamma^2 G^2 \delta}{4\pi^2 f^2} \qquad [2.1]$$

Here γ is the nuclear magnetogyric ratio, G the maximum gradient amplitude, δ the gradient duration, and f the diffusion gradient oscillation frequency. Based on the

equivalence of b-values between OGSE and PGSE sequences (20), the effective diffusion time (Δ_{eff}) for a cosine-modulated OGSE sequence is:

$$\Delta_{\text{eff}} = \frac{1}{4f} \qquad [2.2]$$

Using a Gaussian phase approximation (50,51), which is accurate enough for most practical applications (48), the measured ADC for diffusion inside impermeable cylinders can be expressed as

$$\begin{aligned} \text{ADC}(f,D,R) = 8\pi^2 \sum_k \; & \frac{B_k \lambda_k^2 D^2 f^2}{\delta(\lambda_k^2 D^2 + 4\pi^2 f^2)^2} \times \\ & \left\{ \frac{\delta(\lambda_k^2 D^2 + 4\pi^2 f^2)}{2\lambda_k D} - 1 + \exp(-\lambda_k D\delta) + \exp(-\lambda_k D\Delta)(1 - \cosh(\lambda_k D\delta)) \right\} \end{aligned} \qquad [2.3]$$

where D is the free diffusion coefficient, R is the cylinder radius, Δ is the gradient separation, B_k and λ_k are radius-dependent coefficients (47,52).

$$B_k = \frac{2(R/\mu_k)^2}{\mu_k^2 - 1} \quad \text{and} \quad \lambda_k = \left(\frac{\mu_k}{R} \right)^2 \qquad [2.4]$$

where μ_k is the k^{th} root of $J_1'(\mu) = 0$ and J_1 is a Bessel function of the first kind. Note that similar expressions describe diffusion inside spheres. The ADC depends strongly on the ratio of the time required to diffuse across the space compared to the period of the gradient. In general we can identify three distinct regimes:

when $f >> \frac{D}{R^2}$ there is very little dependence on the radius,

when $f << \frac{D}{R^2}$ the ADC should vary approximately as R^4.

The intermediate regime occurs when $f \sim \frac{D}{R^2}$. Note that for tissues if $D \approx 1$ μm^2/ms then this regime spans the range of frequencies readily accessible for imaging for structures of a few microns in size. The rate of frequency-dependent changes in ADC (Δ_fADC = ∂ADC/∂f) can be readily obtained numerically, and will be shown to first increase and then decrease with frequency. If we define f_0 as the inflection frequency at which Δ_fADC reaches its maximum, the corresponding RMSD can be calculated as

$$\text{RMSD}(f_0) = \sqrt{2D\Delta_{\text{eff}}} = \sqrt{\frac{D}{2f_0}} \qquad [2.5]$$

Using the theoretical expressions, the behavior of Δ_fADC with frequency, radius and D were evaluated.

Simulation

In biological tissues, Δ_fADC may be affected by multiple factors, including cell size, cell membrane permeability, intrinsic diffusion coefficient, the presence of organelles and intracellular water fraction. Moreover, because of limitations on gradient hardware and T_2 relaxation, previous experimental studies have usually acquired data over only a narrow range of frequencies (typically < 200 Hz) (19,23,28,44). Thus, computer simulations were performed to study the effects of radius (R), intracellular intrinsic diffusion coefficient (D_{in}), and intracellular water fraction (f_{in}) on the measured Δ_fADC. The simulations used an improved finite difference method (22,53) and tissues were modeled as impermeable cylinders regularly and closely packed on a hexagonal lattice. Initial parameters were: D_{in} = 1 μm^2/ms, extracellular intrinsic diffusion coefficient D_{ex} = 2 μm^2/ms, R = 3 μm, and f_{in} = 76%. R, D_{in}, and f_{in} were then varied individually to study their effects on ADC measurements. The values of ADC were simulated at PGSE(δ/Δ = 3/50 ms), OGSE(50 Hz), and OGSE(100 Hz). Δ_fADC at f = 75 Hz was approximated as:

$$\Delta_f \mathrm{ADC}(75\ \mathrm{Hz}) \approx \frac{\mathrm{ADC}(100\ \mathrm{Hz}) - \mathrm{ADC}(50\ \mathrm{Hz})}{100\ \mathrm{Hz} - 50\ \mathrm{Hz}} \quad [2.6]$$

In vitro cell experiments

Murine erythroleukemia (MEL) and human promyelocytic leukemia K562 cells were purchased from American Type Culture Collection (ATCC, Manassas, VA). Once enough cells were cultured, they were collected and washed with phosphate-buffered saline (PBS), and then fixed with 4% paraformaldehyde in PBS for over 2 hours. After fixation, cells were centrifuged at 200 g for 2 minutes in a 0.65ml Eppendorf tube to form a pellet, and all the liquid on the top was then carefully removed. There were four samples of each cell type. Using light microscope images, cell radii were estimated to be 5.75 ± 0.51 and 9.49 ± 0.57 μm for MEL and K562 cells, respectively.

NMR diffusion measurements were performed on an Agilent/Varian 7T MRI system with a 12 mm Doty micro-gradient coil. An apodised cosine-modulated OGSE

sequence (20) with a gradient duration of 25 ms was used to acquire temporal ADC spectra from 40 Hz to 360 Hz. An additional PGSE-based ADC was also measured with δ/Δ = 4/52 ms. For each diffusion frequency/time, the ADC was calculated from four b-values evenly distributed from 0 to 0.75 ms/μm^2. Other parameters were: TR = 5 s, NEX (number of excitations) = 1, receiver bandwidth = 50 kHz, spectral resolution = 390.625 Hz, TE = 60 ms. The sample temperature was maintained at ~ 17 ^{o}C using a cooling water circulation system.

Ex vivo animal experiments

Brain, kidney, and liver samples were freshly excised from six female Athymic nude mice (28 – 35 g) after intravascular perfusion and euthanasia. Tissue samples were stored in 10% formalin for more than ten days. The samples were then washed in phosphate-buffered saline solution for one week prior to MRI study to wash out fixatives and restore T_2. For each MRI scan, one sample was put inside a 10-mm NMR tube and immersed in fomblin to reduce susceptibility effects and prevent dehydration.

MR images were acquired on the same scanner as used for the in vitro cell experiments. All images were acquired using a 2-shot echo-planar imaging sequence. For each sample, PGSE data were acquired with δ/Δ = 3/50 ms, while OGSE data were acquired with six oscillating frequencies evenly distributed from 50 to 300 Hz with a gradient duration of 20 ms. Other parameters were: TR = 5000 ms, TE = 67 ms, NEX = 8, 10 diffusion directions, b-value = 0.8 ms/μm^2, FOV = 10 × 10 mm, slice thickness = 1 mm, matrix size = 64 × 64, zero-filled to 128 × 128. The maximum gradient strength used in this study was 1.42 T/m. ADC and Δ_fADC(75 Hz) values were calculated in a pixel-by-pixel manner, and further analyses were performed on regions of interest (ROIs) which were manually selected in brain cortex, kidney cortex, and liver.

Results

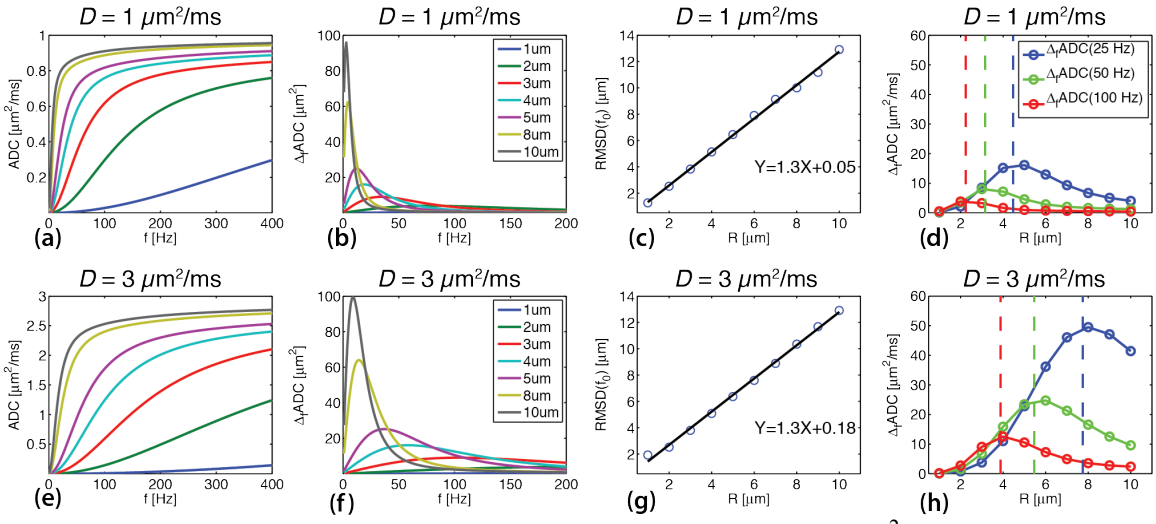

Fig 2.1 The changes of ADC, Δ_fADC and RMSD(f_0) with D = 1 μm^2/ms (**a**,**b**,**c**,**d**) and D = 3 μm^2/ms (**e**,**f**,**g**,**h**). (**a**) and (**e**) show the ADC spectra with R ranging from 1 to 10 μm. The corresponding Δ_fADC spectra are shown in (**b**) and (**f**). f_0 is the frequency at which Δ_fADC reaches its maximum. (**c**) and (**g**) show the linear fitting between RMSD(f_0) and the cylinder radius R, fitted parameters are also provided. The changes of Δ_fADC with R at frequencies 25, 50 and 100 Hz are shown in (**d**) and (**h**), the vertical dashed lines represent the corresponding values of RMSD.

Fig 2.1 shows the numerically calculated values of ADC, Δ_fADC and RMSD(f_0) based on Eqs. [2.3-2.5] for two values of D. It is evident that Δ_fADC is not a monotonic function of f. Δ_fADC increases with increasing f at low frequencies but drops after reaching a maximum at $f = f_0$. Fig 2.1(b) and 2.1(f) suggest that f_0 shifts to higher frequency as the free diffusion coefficient D increases. This is consistent with Eq.[2.3] which predicts, under some simplifying assumptions, that f_0, the inflection point of the spectrum, occurs at a value proportional to $\frac{D}{R^2}$. The RMSD at f_0 (RMSD(f_0)) is thus found to vary linearly with the cylinder radius. If the ADC spectra were acquired and f_0 were identified, the cylinder radius R could be directly estimated as suggested by Fig 2.1(c) and 2.1(g). In practice, due to gradient hardware and relaxation limitations, only a narrow range of ADC spectra may be obtained. Fig 2.1(d) and 2.1(h) show the changes of Δ_fADC with R at three different oscillating frequencies (f = 25, 50 and 100 Hz). The

corresponding effective diffusion times are 10, 5 and 2.5 ms respectively, and the vertical dashed lines represent the corresponding RMSDs. Δ_fADC is not a monotonic function of R, and becomes larger when the cylinder radius R is close to the corresponding RMSD. The range of sizes over which there is a monotonic increase in Δ_fADC with R increases with increasing D and diffusion times.

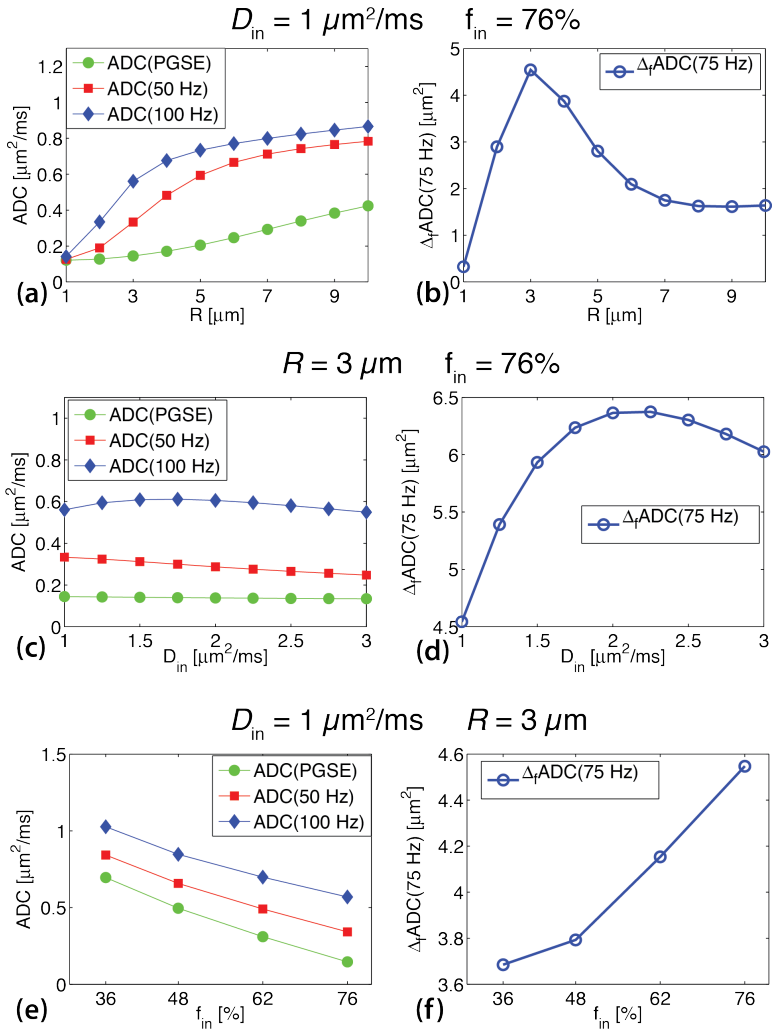

Fig 2.2 The simulated changes of ADC and Δ_fADC(75 Hz) as a function of R (**a**,**b**), D_{in} (**c**,**d**), and f_{in} (**e**,**f**). The effects of R and D_{in} are in good agreement with the theoretical predictions.

Fig 2.2 shows the simulated effects of R, D_{in} and f_{in} on ADC and Δ_fADC(75 Hz). As shown in Fig 2.2(a), ADC increases with increasing R, but the rate of increase is diffusion time/frequency dependent. Consistent with Figs 2.1(d), Δ_fADC(75 Hz) reaches

its maximum when R is close to the RMSD at D_{in} = 1 μm^2/ms and f = 75 Hz. Fig 2.2(d) shows that Δ_fADC(75 Hz) obtains its maximum at D_{in} = 2.25 μm^2/ms, the corresponding RMSD is 1.3 times larger than the cylinder radius (R = 3 μm). The changes of Δ_fADC(75 Hz) with D_{in} are in good agreement with the results in Fig 2.1(b)(c)(f) and (g). Whether D_{in} or f is varied, Δ_fADC reaches its maximum when the RSMD is about 1.3 times larger than R (Fig 2.1(c)).

For a two pool model in which the extracellular intrinsic diffusion rate is set to be higher than the intracellular rate, it is not surprising that Δ_fADC(75 Hz) depends on the intracellular fractional volume and the average ADC decreases. In our simulation, Δ_fADC(75 Hz) increases by about 25% when f_{in} increases 36% to 76%. It should be noted that Δ_fADC(75 Hz) may decrease with increasing f_{in} in some cases (data not shown).

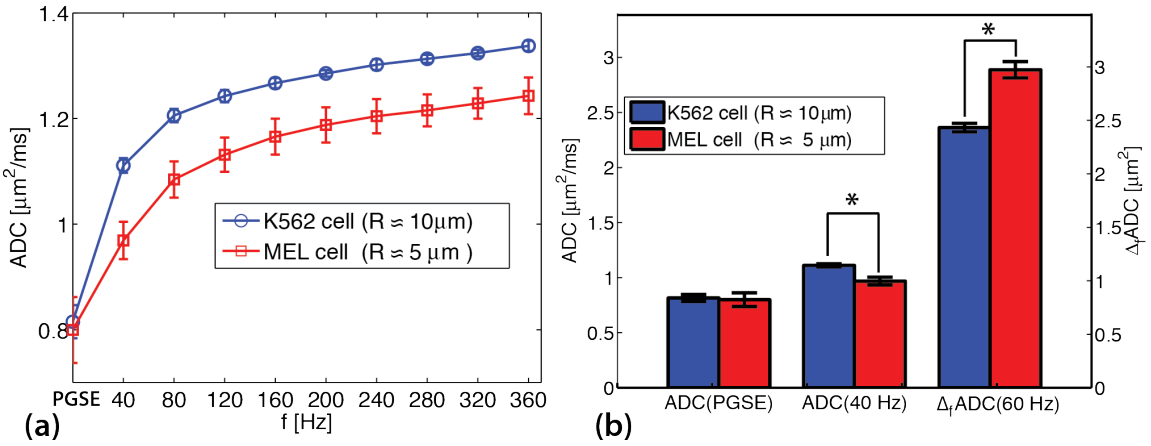

Fig 2.3 The measured ADC spectra for MEL and K562 cells (**a**). Comparisons of ADC(PGSE), ADC(40 Hz), and Δ_fADC(60 Hz) for those two cell types (**b**). The error-bars indicate the inter-subject standard deviations. Statistical significance was evaluated using the paired-sample t-test (* $p < 0.005$).

The measured ADC spectra for MEL and K562 cells are shown in Fig 2.3(a). Fig 2.3(b) shows the comparisons of ADC and Δ_fADC between those two cell types. Δ_fADC at 60 Hz was interpolated from two ADC values at 40 and 80 Hz. Though the K562 cell radius (R ~ 10 μm) is about twice as large as that of MEL cells (R ~ 5 μm), ADC(PGSE) is unable to distinguish them from each other. However, at shorter diffusion times, the ADC values of K562 cells are significantly higher than that of MEL cells ($p < 0.005$),

which is in agreement with their size difference. At 17 °C, the intracellular intrinsic diffusion coefficient D_{in} is estimated to be about 1 μm^2/ms (54). Consistent with Fig 1(a), the ADC spectrum of K562 cells increases faster at relatively low frequencies (< 40 Hz) than that of the MEL cells. However, at a higher frequency (f = 60 Hz), the RMSD is only 2.9 μm and smaller than the cell radii. Then, as predicted, Δ_fADC(60 Hz) for K562 cells (R ~ 10 μm) is smaller than that of MEL cells (R ~ 5 μm).

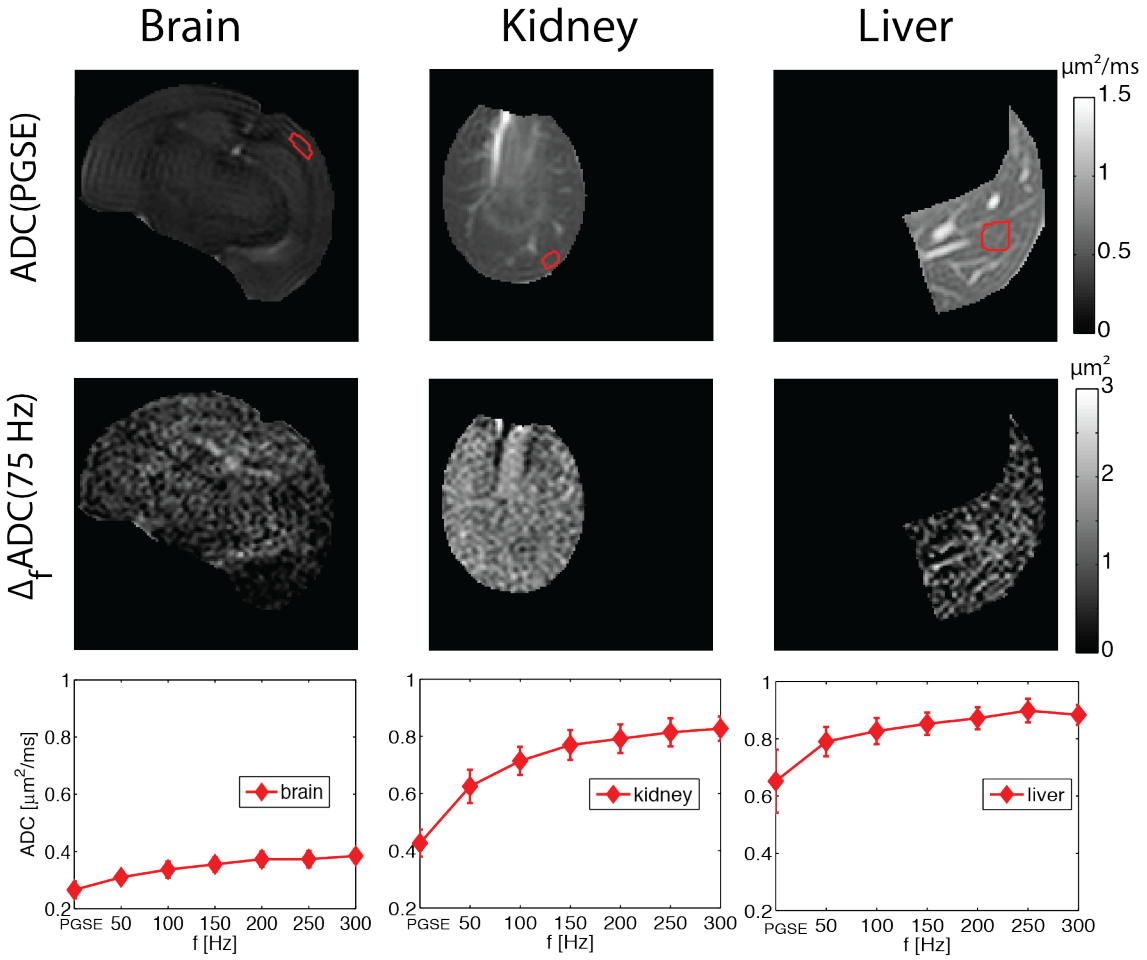

Fig 2.4 ADC(PGSE) maps, Δ_fADC(75 Hz) maps, and ADC spectra for the brain, kidney, and liver. ROIs are shown on the ADC(PGSE) maps. The error-bars represent the standard deviations for six samples.

Fig 2.4 shows the measured ADC(PGSE) and Δ_fADC(75 Hz) maps, and ADC spectra, for brain, kidney, and liver tissues. Consistent with previous reports (27,28,42), Δ_fADC(75 Hz) highlights the granular cell layer of the dentate gyrus (GrDG) in the brain

hippocampus. Different from the ADC(PGSE) map, Δ_fADC(75 Hz) shows almost no contrast for the kidney cortex and medulla, which suggests that the restricting compartments differ in cell density or other ways but may share similar restricting sizes. Fig 2.5 shows the ROI-based ADC(PGSE) and Δ_fADC(75 Hz) values. Both ADC(PGSE) and Δ_fADC(75 Hz) differ between tissues. Typical cell sizes for brain, kidney, and liver are usually 1-3 (55,56), 10-20 (57,58), and 15-30 μm (59), respectively, and cell density is expected to vary inversely with size in close packed tissues. In the regime of frequencies and sizes examined the changes of Δ_fADC(75 Hz) seen are in agreement with those in Fig 2.1(d), so a large value of Δ_fADC(75 Hz) does not always mean a large restricting size but depends on other experimental variables.

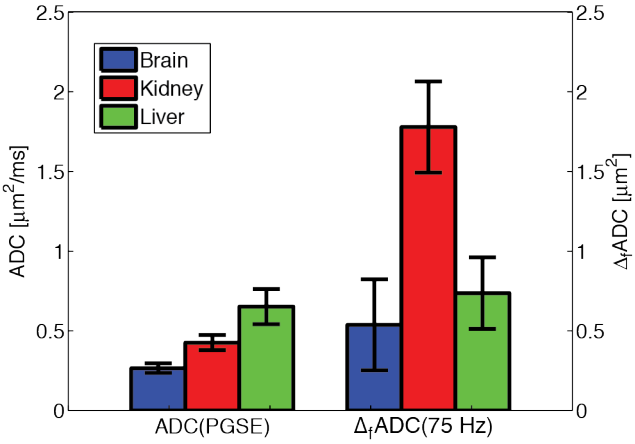

Fig 2.5 Comparisons of ADC(PGSE), and Δ_fADC(75 Hz) for brain, kidney, and liver tissues.

Discussion

This study re-examined the restricted diffusion within an impermeable cylinder under cosine-modulated OGSE sequences. Our emphasis was to interpret the dispersion rate of ADC with oscillating frequency at relatively low frequencies. Whereas ADC spectra increase continuously with frequency, they also show inflections so that Δ_fADC is not a monotonic function of frequency but reaches a maximum when the second derivative is zero. This occurs at a frequency that in practice is proportional to the cylinder area of R^2, when the RSMD is about 1.3 times larger than the cylinder radius R.

The RSMD value at the point of inflection is itself a reliable indicator of compartment size and varies in direct proportion to R.

At long diffusion times, water in tissues whose cells have non-zero permeability may have encountered restricting barriers or exchanged between the intra- and extracellular spaces many times. The measured ADC then may be relatively insensitive to the restricting size and is mainly determined by cell density and permeability (60). At extremely short diffusion times, only a small fraction of water may experience the restrictions or hindrances introduced by barriers. The measured ADC then is close to the free diffusion coefficient, which also cannot reflect information on the restricting size. However, when the distance moved in the diffusion time is comparable with the restricting size, the measured ADC varies strongly with the dimensions between the restricting barriers (18). The frequency at which Δ_fADC reaches its maximum is then an essential feature of ADC spectra that correlates with intrinsic tissue structure.

The relation between Δ_fADC and R derived from the theory can be used to explain previous reports (27,28,42). Typical sizes for cells in the cerebellar granule layer (CBGr), the granule layer of the dentate gyrus (GrDG), and hippocampal pyramidal layer (Py) are 5-10 (61), 10-18 (62), and 20 μm (28,63), respectively. Using the relation between Δ_fADC and R described above, it is not surprising to observe that CBGr had a larger Δ_fADC(75 Hz) than GrDG, which in turn had a larger Δ_fADC(75 Hz) than Py (28). Another previous study observed that the values of Δ_fADC(75 Hz) decreased in CBGr but increased in brain cortex after mouse death (42). Though the values of Δ_fADC(75 Hz) changed in opposite directions in those regions, both of them were consistent with increased cell size (55,64) and decreased diffusion coefficient (65-67) after death. CBGr has a larger radius than the RMSD, so the value of Δ_fADC(75 Hz) would decease once cell radius increases. However, the neuronal radii in brain cortex are relatively smaller than the RMSD, so the increased neuronal radii would be more close to the RMSD after death.

This study suggests that measuring ADC spectra at multiple diffusion frequencies/times around f_0 is key to obtaining structural dimensions from diffusion measurements. Axon sizes in the central nervous system may be as small as 2 μm, such as those in the spinal cord white matter tracts and corpus callosum (68). OGSE

measurements with higher frequencies (> 200 Hz) would be more sensitive to those small axons than conventional PGSE-based measurements (34). However, for cell sizes in the range of 5 to 20 μm or larger, measurements at much lower frequencies, such as can be achieved using PGSE sequences, may be more suitable. The relative performance of different sequences may be readily interpreted in terms of their temporal spectral representations.

Conclusion

In this study, the theory of water diffusion within an impermeable cylinder was re-examined to derive the relation between Δ_fADC and restricting size. The results indicate that Δ_fADC passes through a maxium when the restricting radius R is close to the corresponding RMSD, and the frequency of this inflection is a reliable indicator of compartment size. However, single values of Δ_fADC should be interpreted with caution, though for low frequencies and larger structures Δ_fADC increases with size. This study may help better understand the information revealed by the behavior of ADC with frequency.

CHAPTER III
TIME-DEPENDENT INFLUENCE OF CELL MEMBRANE PERMEABILITY ON MR DIFFUSION MEASUREMENTS

Abstract

Cell membrane permeability has an important influence on MR diffusion measurements. For example, increased cell membrane permeability following apoptotic cell death[1] can significantly increase the apparent diffusion coefficient (ADC) because water is no longer as restricted. Although several models have previously been developed to account for permeability effects, recent studies that have used diffusion data to extract axon or cell sizes have usually ignored water exchange between the intra- and extracellular spaces for simplicity. This approximation assumes that the cell membrane permeability is small, so the intracellular lifetime is much longer than the diffusion time (Δ_{eff}). Intuitively, the influence of cell membrane permeability should be less pronounced at shorter diffusion times. However, the precise nature of this time-dependent influence has not been comprehensively quantified. In the current study, we developed an experimental protocol to selectively alter cell membrane permeability, and then investigated its influence on diffusion measurements over a broad range of effective diffusion times (0.4 ms < Δ_{eff} < 3000 ms). The influence of cell membrane permeability on the measured ADCs is negligible in OGSE measurements at moderately high frequencies. By contrast, cell membrane permeability has a significant influence on ADC and quantitative diffusion measurements at low frequencies such as those sampled using conventional pulsed gradient methods.

Introduction

The self-diffusion of water molecules in biological tissues is restricted or hindered by intrinsic microstructures, and magnetic resonance methods for measuring diffusion obtain only an apparent diffusion coefficient (ADC) which reflects an integrated, average effect of restrictions and hindrances at multiple scales. In practice the measured ADC of real tissues may depend on the choice of diffusion gradient factors and diffusion time, and has been reported to be affected by multiple biophysical properties,

including but not limited to cell size (69), cell membrane permeability (60), intracellular and extracellular diffusion coefficients (70), cellular volume fraction (71), nuclear size (72) and organelles (73). The sensitivity of diffusion measurements to such microstructural features provides an opportunity to non-invasively probe pathologic changes caused by various diseases, which forms the basis for the widespread use of diffusion-based MRI clinically, such as detecting stroke (35), predicting tumor response to therapy (36-38), and quantifying white matter structures (74). However, variations in ADC usually reflect multiple factors that may simultaneously influence diffusion, so that they rarely allow a unique interpretation of underlying causes. To assist better interpretation of diffusion data, the precise influence of individual factors on diffusion measurements need to be understood, and methods that simplify this multifactorial dependence may have practical advantages. In the current study, we focus on the influence of cell membrane permeability, and show that its influence may be substantially reduced using short diffusion times.

Most human cells have a high capacity for rapid water transport that is highly regulated, essential for normal biological function and often altered in a variety of disease processes including cancer (75). Cell membranes have only finite permeability and therefore act as restricting barriers to self-diffusing water molecules in biological tissues. The influence of cell membrane permeability on diffusion measurements has been previously investigated via theoretical modeling and computer simulations (60,76,77), cell culture experiments (77-80), and MR imaging *in vivo* (81-83). However, these previous studies had several limitations. First, they all considered diffusion over relatively long diffusion times, so that all water in the sample had a reasonable chance of interacting one or more times with a membrane. These previous measurements used either pulsed gradient spin echo (PGSE) or stimulated echo (STEAM) sequences, and due to practical hardware limitations, the diffusion times were necessarily long. Note that theoretical modeling and computer simulations have predicted that, in larger cells, the influence of cell membrane permeability should be negligible when very short diffusion times are involved because little of the water volume would then interact with the restricting membranes (60), but this behavior will depend on the surface to volume ratio of cells and has not been experimentally validated. Second, previous studies usually

investigated the influence of cell membrane permeability by blocking water channels (77,78,81), whereas increases in cell membrane permeability are more physiologically relevant in biological tissues when pathological changes occur (84-87). Moreover, the blockage of water channels in live cells (78) or animals (81) can cause osmotic stress variations that may lead to apoptosis, during which cell size and other cellular features may vary, so these experimental approaches may result in variations in multiple cellular microstructural properties simultaneously, which complicates their interpretation.

To investigate the precise relationship between cell membrane permeability and diffusion measurements, two modifications to previous approaches were employed in the current study. First, we used oscillating gradient spin echo (OGSE) sequences to achieve short diffusion times (0.42 – 5 ms), combined with stimulated echo (STEAM) sequences to achieve longer diffusion times (11 – 2999 ms), so that a broader range of diffusion times could be obtained. There has recently been increasing interest in implementing OGSE methods with short diffusion times to probe microstructure at small length scales in tissues (18,24), but the influence of cell membrane permeability on OGSE measurements has not been investigated before except in simulations (22). Second, a different experimental approach was used to selectively increase the cell membrane permeability (i.e. to decrease intracellular exchange lifetime τ_{in}) without altering other cellular features. Compared with previous studies increasing τ_{in} by only 7 ms (78), a wider range of τ_{in} (~ 82 – 317 ms) was achieved. This provided a more comprehensive assessment of the influence of cell membrane permeability with greater physiological relevance. By these means, a comprehensive investigation of the influence of cell membrane permeability on diffusion measurements was performed using both computer simulations and experiments *in vitro* over a broad range of diffusion times without interference from other cellular changes, particularly changes in the cell size.

Methods

Selective change of cell membrane permeability

Saponin is a natural detergent that selectively removes membrane cholesterols (88) and produces small pores (40 – 50 Å) in cell membranes (89). Water molecules can diffuse through these pores and hence the cell membrane permeability is effectively

enhanced. Note that saponin does not cross cell membranes, so the intracellular structure, e.g. nuclear envelope, is unlikely to be altered by saponin treatment. To prevent other side effects that may be induced by saponin treatment, only fixed cells were used in the current study. By such a means, cell membrane permeability was increased selectively without altering other cell properties, and this in turn provides an appropriate model system to investigate the precise influence of membrane permeability on diffusion measurements.

Sample Preparation

Human myelogenous leukemia K562 cells were purchased from American Type Culture Collection (ATCC, Manassas, VA) and cultured in Dulbecco's modified eagle medium (DMEM) supplemented with 10% fetal bovine serum (FBS), 50 U/ml penicillin, and 50 μg/ml streptomycin (Invitrogen, CA) under standard culture conditions in a humidified incubator maintained at 5% CO_2 and 37 °C. Once enough cells were cultured, they were collected and washed with phosphate-buffered saline (PBS), and then fixed with 4% paraformaldehyde in PBS for about 2 hours. After fixation, cells were washed and divided into three groups, each treated with vehicle (control), low (0.025% w/v) and high (0.05% w/v) concentrations of saponin. Briefly, 10% saponin was added to the fixed cells (at about 10 million cells per ml) to reach a final saponin concentration of 0.025% or 0.05%. After 30 minutes of incubation at room temperature, approximately 30 million cells were centrifuged at 6000 g for 2 minutes in a 0.65ml of Eppendorf tube to form a pellet, and all the liquid on the top was then carefully removed. The estimated intracellular volume fraction was around 72%. There were six samples in each group. To confirm that the saponin treatment did not alter cell size distribution, aliquoted samples were spotted on glass slides and directly imaged with phase contrast microscopy. Over 100 cells were measured for each sample. Cell radii were 9.61 ± 0.66, 9.46 ± 0.73, 9.49 ± 0.56 μm for cell samples with saponin concentrations of 0, 0.025%, 0.05%, respectively.

MR experiments

NMR diffusion measurements were performed on an Agilent/Varian 7T MRI system with a 12 mm Doty micro-gradient coil. Temporal ADC spectra were acquired

over a broad range of frequencies and effective diffusion times (0.42 ms ≤ Δ_{eff} ≤ 3000 ms) with five b-values evenly distributed from 0 to 0.6 ms/μm^2. The diffusion gradients were applied simultaneously on three axes, the maximum gradient strength used was 1.42 T/m. Short diffusion times were achieved using OGSE sequences with apodised cosine-modulated gradient waveforms with a duration of 20 ms on either side of a refocusing pulse. Twelve oscillating frequencies (*f*) were evenly distributed from 50 Hz to 600 Hz, corresponding to 12 effective diffusion times from 0.42 ms to 5 ms ($\Delta_{eff} = \frac{1}{4f}$). Long diffusion times (equivalent to sampling low frequencies) were achieved using STEAM with a pulsed gradient duration δ = 3 ms. Twelve different effective times from 11 ms to 2999 ms were acquired by varying the mixing time TM but keeping the other parameters the same. A 3 mm axial slice crossing the middle of cell pellets were excited for the collection of NMR signals. By such a means, potential B_1 inhomogeneity and gradient non-linearity effects at the edges of the cell pellets were avoided. Other parameters were: TR = 5 s, NEX (number of excitations) = 2, the number of dummy scans = 2, receiver bandwidth = 50 kHz, spectral resolution = 390.625 Hz, TE = 50 or 15 ms for OGSE and STEAM sequences, respectively. The sample temperature was maintained at ~ 17 ^{o}C using a cooling water circulation system. The acquisition time of each diffusion frequency/time was about 1 min.

The intracellular exchange lifetimes were estimated using constant gradient (cg-) experiments as described by Meier et al. (76,82). With the same STEAM sequence, diffusion weighting was achieved by keeping δ = 10 ms and varying the gradient separation Δ in 30 increments. The maximum Δs were 542, 310, 165 ms for cell samples with saponin concentrations of 0, 0.025%, 0.05%, respectively. Each experiment was repeated with two different gradient amplitudes, g = 5 and 150 mT/m. The higher gradient amplitude data were normalized by the lower gradient amplitude data to compensate for any T_1 relaxation effects (82). After normalization, the ADC of the slowly decaying component (D_B) was determined by linear regression using the last 10 data points (shown in Figure 3.1). The intracellular exchange lifetime τ_{in} was then derived as (76)

$$\tau_{in} = \frac{1}{\gamma^2 g^2 \delta^2 D_B} \qquad [3.1]$$

where γ is the nuclear magnetogyric ratio. The cell membrane permeability P_{m} can then be derived as (76,90)

$$P_{\mathrm{m}} = \frac{3\tau_{in}}{R} - \frac{R}{5D_{\mathrm{in}}} \qquad [3.2]$$

where R is the cell radius and D_{in} is the intracellular intrinsic diffusion coefficient.

Simulations

Computer simulations were performed based on the cell membrane permeabilities derived from experiments, i.e. 0, 0.01, 0.019, 0.044 μm/ms. The simulations used an improved finite difference method (22,53) and tissues were modeled as spherical cells regularly packed on a face-centered cube (FCC) lattice with intracellular fraction of 68%. The extracellular intrinsic diffusion coefficient was assumed to be the same as the free water diffusion coefficient at 20 ^{o}C, i.e. D_{ex} = 2 μm^2/ms (91), and the intracellular intrinsic diffusion coefficient D_{in} was assumed to be one-half of the free water diffusion coefficient (54), i.e. D_{in} = 1 μm^2/ms. Five different cell radii, R = 2.5, 3.75, 5, 7.5, 10 μm, were simulated to investigate the coupled influence of cell size and membrane permeability. The MR sequence parameters were the same as were used in the experiments.

Results

Figure 3.1 shows the signal intensities measured in cg-experiments as a function of b-value for cells with three different concentrations of saponin. Note that the error-bars, as determined by the standard deviations of six samples in each group, were smaller than the symbol sizes in most cases. The straight lines represent the linear fitting for the natural logarithm of the last 10 data points and their b-values (82). The samples treated with higher concentrations of saponin showed more rapid signal decays, which indicated larger ADC and higher cell membrane permeability. The τ_{in}'s were estimated using Eq.[3.1] to be 317 ± 17 ms, 183 ± 13 ms, and 82 ± 4 ms for the cell samples with saponin concentrations of 0, 0.025%, and 0.05%, respectively. With the approximation that the

intracellular intrinsic diffusion coefficient D_{in} is about one-half of the free water diffusion coefficient at the same temperature (54), D_{in} was assumed to be 1 $\mu m^2/ms$, and the corresponding mean cell membrane permeabilities were then estimated using Eq.[3.2] as 0.011, 0.019, and 0.044 μm/ms.

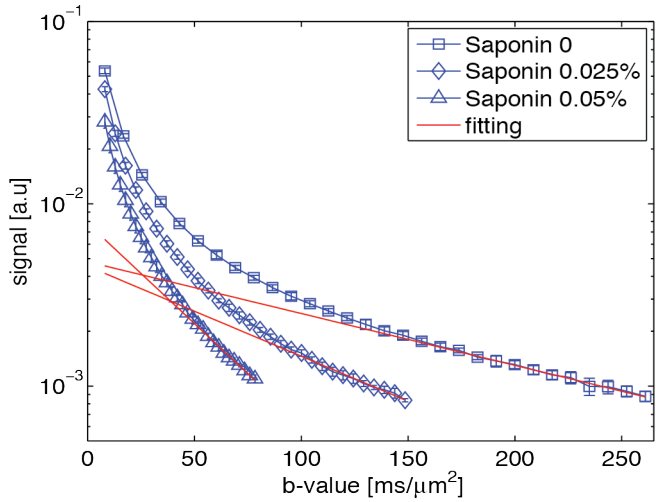

Figure 3.1 Signal intensities as a function of b-value for cg-experiments with different concentrations of saponin. The red straight lines indicate the best linear regressions of the slowly decaying components at high b-values. The error-bars represent the inter-sample standard deviations in each group (n = 6).

Figure 3.2 shows the simulated ADC spectra for different cell sizes with different permeabilities. The ADC values at $\Delta_{eff} > 10$ ms were simulated for conventional pulsed gradient sequences, while those at $\Delta_{eff} < 5$ ms used cosine-modulated OGSE waveforms. As expected, ADC was observed to increase with increasing permeability, but it is evident that the influence of membrane permeability on ADC was very different at different diffusion times. When Δ_{eff} was long (> 300 ms), ADC became relatively independent of Δ_{eff}, and significant differences in ADC values were apparent between groups of varying permeabilities. This is consistent with previous results showing that ADC is mainly determined by membrane density and permeability at long diffusion times (60). When Δ_{eff} decreased from 100 ms to 1 ms, ADC changed dramatically for typical cell sizes (2.5 μm < R < 10 μm) with typical cell membrane permeabilities (0 < P_m < 0.05 μm/ms) (79,92). Moreover, the ADC differences between groups became smaller with

decreasing Δ_{eff}. For typical PGSE-based measurements with 10 ms < Δ_{eff} < 60 ms, the effects of permeability were usually not negligible. But for typical OGSE-based measurements with oscillating frequency as high as 200 Hz (19,20), the simulated ADCs were almost independent of permeability. When Δ_{eff} < 1 ms, the ADC differences between groups disappeared indicating ADC values were insensitive to permeability with short diffusion times, as was predicted by computer simulations (22,60).

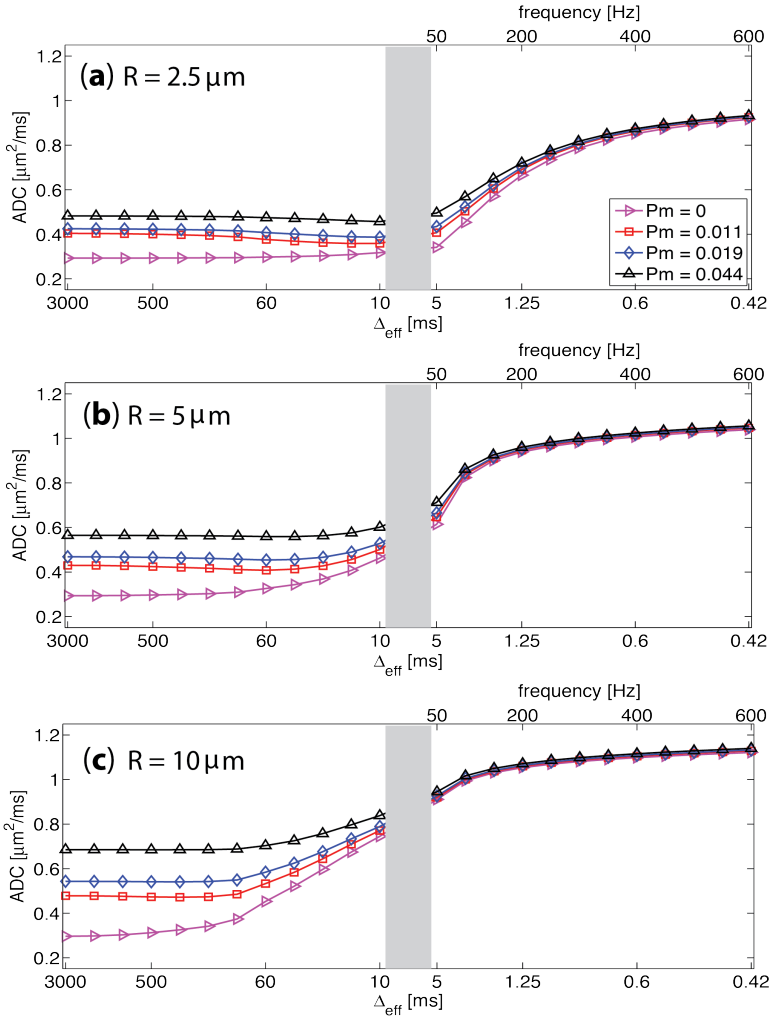

Figure 3.2 The simulated apparent diffusion spectra for different cell sizes with radius = 2.5 µm (**a**), 5 µm (**b**), and 10 µm (**c**) with cell membrane permeability P_m ranging from 0 to 0.044 µm/ms. The effective diffusion time (Δ_{eff}) is shown on the lower X-axis. The oscillating frequency is shown on the upper X-axis for the OGSE cases. Note that Δ_{eff} is displayed in the reversed direction.

Figure 3.3 shows the simulated dependence of ADC on cell size with different cell membrane permeabilities at two typical diffusion times. When Δ_{eff} = 30 ms, which is typical for pulsed gradient diffusion measurements, the dependence of ADC on cell size varies significantly with different cell membrane permeabilities. For example, the ADC of impermeable cells (P_m = 0) with a cell radius of 5 μm was calculated to be similar (1.7% difference) to that of cells with a radius of 2.5 μm and a cell membrane permeability of 0.011 μm/ms (see the two solid markers in Figure 3.a). This indicates that the cell size may be significantly overestimated if the cell membrane permeability is not taken into account in quantitative diffusion measurements. By contrast, when Δ_{eff} = 1.25 ms (f = 200 Hz), which is readily achievable on current animal scanners, the dependence of ADC on cell size is insensitive to cell membrane permeability, which is desirable for accurate estimation of cell size from diffusion measurements.

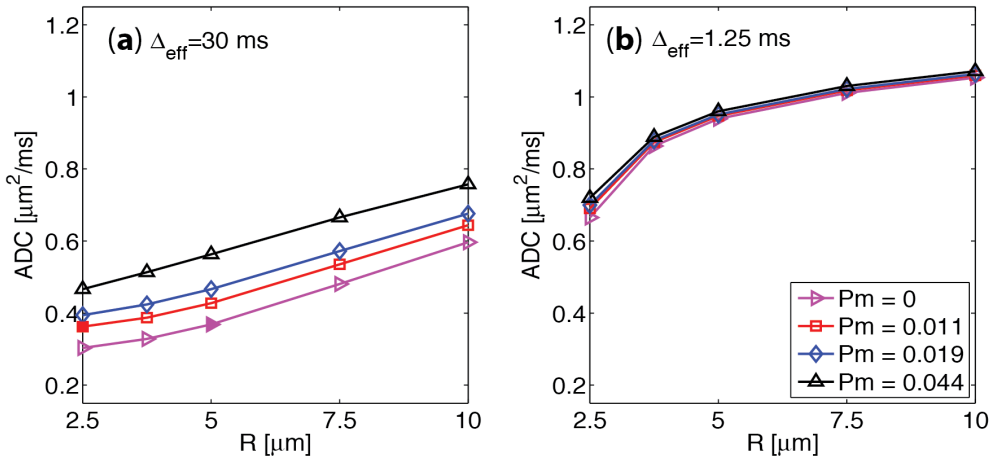

Figure 3.3 The simulated dependence of apparent diffusion coefficient (ADC) on cell radius varies with cell membrane permeability at a long diffusion time of 30 ms (**a**), but is insensitive to permeability at a short diffusion time of 1.25 ms (**b**). The two solid markers in (**a**) represent two ADC values with < 2% difference but with very different cell radii and membrane permeabilities.

Figure 3.4 shows the measured apparent diffusion spectra for cells treated with different concentrations of saponin. The measured ADCs were larger for samples with higher concentrations of saponin because of higher permeabilities. The effects of permeability on the measured ADCs were in agreement with the simulation results shown

in Fig.2. For the sizes of cells investigated here (radius 9.5 ± 0.6 μm), the OGSE-based measurements with shorter Δ_{eff} were much less affected by changes of permeability than PGSE-based measurements. The ADC differences between different groups were less than 10% at Δ_{eff} = 5 ms and became < 5% when Δ_{eff} was smaller than 1.25 ms, indicating no significant differences between ADC values even with various membrane permeabilities.

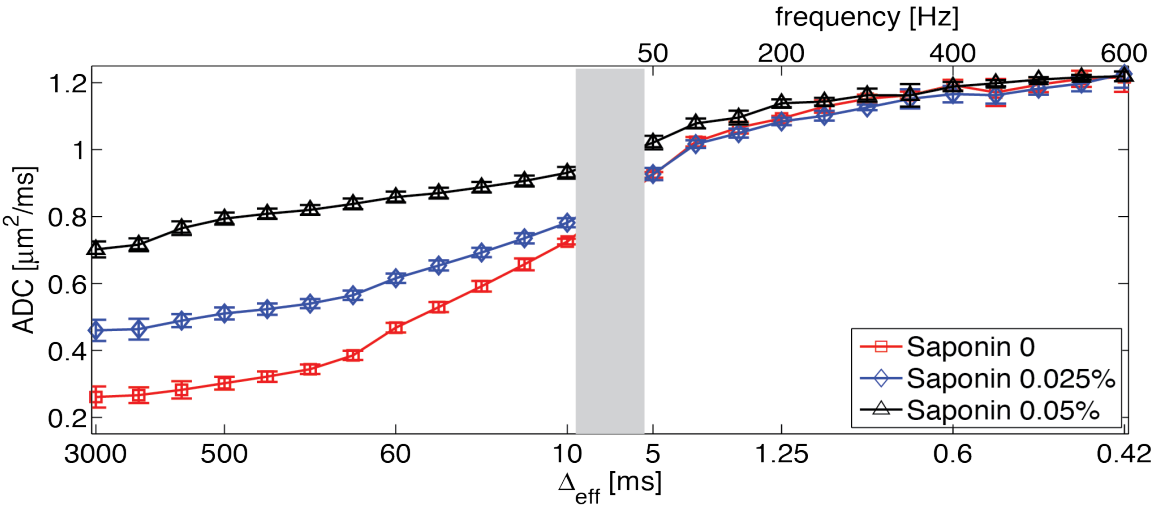

Figure 3.4 The diffusion time (Δ_{eff}) dependent apparent diffusion coefficients (ADCs) of cells treated with different concentrations of saponin and measured by STEAM (left) or OGSE (right). The error-bars represent the inter-sample standard deviation in each group. The effective diffusion time (Δ_{eff}) is shown on the lower X-axis. The oscillating frequency is shown on the upper X-axis for the OGSE measurements. Δ_{eff} is displayed in the reversed direction.

Discussion

The goal of this study was to investigate the influence of cell membrane permeability on MR diffusion measurements over a broad range of diffusion times and physiologically relevant permeabilities, and to demonstrate that the effects of permeability variations can be minimized using short diffusion times. Cells were treated with either of two concentrations of saponin to vary the cell membrane permeability that was calculated from cg-experiments (Figure 3.1) to range from 0.011 μm/ms to 0.044 μm/ms, corresponding to intracellular exchange lifetime τ_{in} 82 – 317 ms. Note that this is a physiologically relevant range for typical τ_{in} of tumor cells and those undergoing

apoptosis. For example, the transmembrane water exchange rate has been reported as 2.9±0.8 s^{-1} (τ_{in} = 344 ± 1.25 ms) for viable human brain tumor (85), and 1.4 – 6.8 s^{-1} (τ_{in} = 147 - 714 ms) for tumor cells undergo apoptosis (84). The saponin treatment at either 0.025 or 0.05% had no detectable effect on the sizes of the fixed cells. The effects of permeability on the measured ADCs were then investigated at a broad range of effective diffusion times (0.42 ms < Δ_{eff} < 3000 ms). The results confirmed that the OGSE measurements are not sensitive to changes of permeability, especially at higher oscillating frequencies. This is an encouraging result for the implementation of OGSE imaging of tissues. For example, ADC values obtained using PGSE measurements are usually suggested as indicators of cellularity and have been widely used to monitor tumor response to treatment (93). However, cell membrane permeability also changes in treated tumors, and has been reported to increase significantly following apoptotic cell death (84), which can then also significantly increase ADC values because water is no longer as restricted (29). This may explain some observations that the ADC and tumor cellularity are not always strongly correlated (36,39,94). Recently, there has been an increasing interest in implementing OGSE sequences to study tissues, including tumors, to probe structural variations at very small length scales (18,23), but the cell membrane is a major restricting barrier to water molecules that may still affect OGSE measurements when the diffusion time is of the order of the time to diffuse across a cell. The current study suggests that OGSE measurements in cells, ranging in size down to a radius of 2.5 μm, are not sensitive to changes in cell membrane permeability; this result implies that ADC values obtained using OGSE sequences with moderately high frequencies (~ 200 Hz) simply reflect the averaged intra- and extra-cellular diffusion properties on small length scales without the influence from cellular-level barriers. Such a conclusion may improve the interpretation of OGSE measurements in cancer and other pathologies. It should be pointed out that, if smaller cells (R < 2.5 μm) were imaged, higher frequencies (> 200 Hz) would be required to minimize the influence of cell membrane permeability on OGSE measurements.

Besides cg-experiments, several other NMR approaches which rely on different relaxation or diffusion properties have also been proposed to measure τ_{in} (79,80,84,95-97). The cg-experiment was chosen in this study because it can be easily implemented

without a need to modify pulse sequences (95) or to add extra contrast agents (97). Over the wide range of b-values used in cg-experiments, the signal decay may not be mono-exponential. The ADC of the slowly decaying component (D_B) at high b-values is mainly determined by the transmembrane flux and the intracellular exchange lifetime τ_{in} can then be derived from Eq.[3.1] (82). However, it should be noted that the estimation of τ_{in} may be slightly biased in this study. As discussed by Meier et al (76), at least two requirements need to be fulfilled for measuring τ_{in} accurately with cg-experiments. First, the derivation of τ_{in} is through the modified Karger model (98), which assumes a long diffusion time ($\Delta \cdot D_{in}/R^2 >> 1$). The maximum Δ for the cells treated with 0.05% saponin was only 165 ms ($\Delta \cdot D_{in}/R^2 \sim 1.65$), which means the long diffusion time assumption was not completely satisfied. Note that the diffusion time could not be further increased due to the limitation of the signal-to-noise ratio (SNR) at long diffusion times. Even for Δ = 165 ms used in the current study, due to the fast signal decays with increasing Δ (Figure 3.1), the corresponding signal was already below 0.1% of the non-diffusion weighted signals. Second, since the stimulated echo cg-experiment requires T_1-weighting correction, the τ_{in} cannot be measured accurately unless intra- and extra-cellular longitudinal relaxations are similar. The measured T_1s for the cell samples were around 2 sec, while T_1 for the pure extracellular PBS was about 3 sec. All of above discrepancies may bias the accurate estimation of τ_{in}, as well as the cell membrane permeability. However, such a bias does not affect the current experimental approach qualitatively, i.e. higher concentration of saponin resulted in higher cell membrane permeability in our experiments.

The comparison between the simulated ADCs (Figure 3.2 e) and the measured (Figure 3.3 a) reveals two discrepancies. First, the simulated ADC values were almost constant when $\Delta_{eff} > 500$ ms, while the measured ADCs dropped slightly with increasing Δ_{eff}. Our observation that ADCs decreased with increasing Δ_{eff} at long diffusion times is consistent with previous results in skeletal muscle (99), and it may be explained by the unordered packing of cells (100). Our simulations were based on a collection of regularly packed spherical cells, but cells are not spherical and, as prepared in these studies, pack randomly and without order. The spatially extended random restrictions result in a long-time tail in the dispersion of ADC with Δ_{eff}, which has been suggested to characterize the

structural disorder (100,101). Second, the simulated ADC values with P_m = 0.044 μm/ms were similar to that of the 0.05% saponin cells measured with P_m of 0.044 μm/ms, but the simulated ADC values with P_m = 0.011 μm/ms were much larger than that of the control cells measured with P_m of 0.011 μm/ms. It may be due to the inaccurate measurements of permeability or the influence of the random packing of cells (100).

Although several models (102) have previously been developed to account for permeability effects, recent studies that have used diffusion data to estimate axon diameters or tumor cell sizes have, for simplicity, usually ignored water exchange between the intra- and extracellular spaces (31,32,34). This assumes that the cell membrane permeability is small, so τ_{in} is much longer than the diffusion time, and consequently only a small fraction of water is exchanged during diffusion measurements. Based on the current simulation results, τ_{in} should be at least 15 times larger than the effective diffusion time, Δ_{eff}, so that exchange could be ignored (ADC difference < 5%). It should also be noted that the influence of permeability is different for different b-values with the same diffusion time. Only small b-values ($\leq$ 0.6 ms/μm^2) were used to measure ADC in this study, where the mono-exponential decay model appeared appropriate. However, the behavior of signal decay with large b-value (> 2 ms/μm^2) would be more complex and constant-time (ct-) experiments cannot be well described by the Karger model (76,103). It has been found that the diffusion measurements for larger b-values are even more sensitive to changes in cell membrane permeability (104).

Supported by simulations and experiments, cosine-modulated OGSE measurements with shorter effective diffusion times are less affected by changes in cell membrane permeability. Thus OGSE should be more specific for detecting other microstructural changes (23-25). Here we should distinguish between the effective diffusion time Δ_{eff} and the total duration of the oscillating gradient waveform Δ_{total}. Water molecules diffuse and experience gradient effects over the total duration of the oscillating gradient waveform. Δ_{total} is usually longer than 40 ms for cosine-modulated gradient waveforms, during which a large fraction of water can exchange between the intra- and extracellular spaces. However, the rapid reversal of the gradient during the time it is on ensures that only the fraction that exchanges during such a period affects the overall ADC. The effective diffusion time Δ_{eff} can be reduced to less than 1 ms by increasing the

oscillating frequency, and the ADCs then mainly reflect the diffusion behavior only over the short effective diffusion time (105). Our simulations and experiments suggest that it is the effective diffusion time that determines the influence of cell membrane permeability on diffusion measurements, i.e. the shorter the effective diffusion time, the smaller the influence of cell membrane permeability. More oscillations at the same frequency increase gradient duration Δ_{total} as well as the diffusion weighting, but have little impact on the influence of membrane permeability.

The focus of this study was the influence of cell membrane permeability, so the effects of D_{in}, D_{ex}, f_{in}, TE and T_2 relaxation were not fully considered. Based on previous simulations (22,71,106), all of them may affect the ADC spectra. In extreme situations where the intra- and extracellular T_2s were much different and the intracellular T_2 was much shorter than TE (e.g. T_{2in}/T_{2ex}/TE = 25/150/40 ms), the ADC values at f = 500 Hz showed considerable decreases as the permeability increased from 0 to 0.05 μm/ms (22). However, after increasing T_{2in} to be the same as T_{2ex} (e.g. T_{2in}/T_{2ex}/TE = 150/150/40 ms), the ADC values at f = 500 Hz were found independent of the cell membrane permeability (22). In the current experiments, the overall T_2 of cell samples was found to be around 130 ms, and TEs (50 ms for OGSE and 15 ms for STEAM) were much shorter than T_2. Therefore, we expect that the influence of TE on our experiments was not significant.

A challenge to translating in vitro experimental results to in vivo studies is that there are significant pathophysiological differences between live tissues and fixed tissues or cell cultures. This is a common problem for all in vitro experiments, not limited to the current study. However, by selectively altering cell membrane permeability, we developed a well-controlled biological test medium to study the precise influence of cell membrane permeability on diffusion MR experiments. Although the pathophysiological differences between live tissues and cell cultures, e.g. intracellular volume fraction, may affect the quantitative results, e.g. the threshold frequency at which the influence of cell membrane permeability on OGSE measurements can be ignored, the qualitative results are still relevant, i.e. the influence of permeability on OGSE measurements will be less pronounced with shorter diffusion times.

Conclusion

In the current study, we developed an experimental protocol to selectively alter cell membrane permeability, and then investigated its influence on diffusion measurements over a broad range of effective diffusion times (0.4 ms < Δ_{eff} < 3000 ms). Stimulated echo acquisitions with pulsed gradients were used to achieve long Δ_{eff} from 11 ms to 2999 ms, while cosine-modulated OGSE methods were used to obtain shorter Δ_{eff} ranging from 0.42 ms to 5 ms. Consistent with computer simulations, the influence of membrane permeability on diffusion measurements is highly dependent on the choice of diffusion time. It can be negligible, but only when the diffusion time is very short, such as the case of cosine-modulated OGSE measurements at moderately high frequency (~ 200 Hz). By contrast, permeability has a major influence on diffusion measurements for intermediate/long diffusion times obtained in typical PGSE measurements. This study improves our understanding of the contrast mechanism of OGSE imaging, and helps elucidate the influence of membrane permeability on PGSE measurements with intermediate diffusion times.

CHAPTER IV

FAST AND ROBUST MEASUREMENT OF MICROSTRUCTURAL DIMENSIONS USING TEMPORAL DIFFUSION SPECTROSCOPY

Abstract

Mapping axon sizes non-invasively is of interest for neuroscientists and may have significant clinical potential because nerve conduction velocity is directly dependent on axon size. Current approaches to measuring axon sizes using diffusion-weighted MRI, e.g. q-space imaging with pulsed gradient spin echo (PGSE) sequences usually require long scan times and high q-values to detect small axons (diameter < 2 μm). The oscillating gradient spin echo (OGSE) method has been shown to be able to achieve very short diffusion times and hence may be able to detect smaller axons with high sensitivity. In the current study, OGSE experiments were performed to measure the inner diameters of hollow microcapillaries with a range of sizes (~ 1.5-19.3 μm) that mimic axons in the human central nervous system. The results suggest that OGSE measurements, even with only moderately high frequencies, are highly sensitive to compartment sizes, and a minimum of two ADC values with different frequencies may be sufficient to extract the microcapillary size accurately. This suggests that the OGSE method may serve as a fast and robust measurement method for mapping axon sizes non-invasively.

Introduction

Mapping the sizes of nerve axons may have significant clinical potential because nerve conduction velocity is directly dependent on axon size (31,107,108). Diffusion MRI provides a non-invasive means to characterize the microstructure of biological tissues, and hence may be suitable for this application. Several approaches have previously been proposed to measure axon sizes using diffusion weighted MRI (31,69,109-116). For example, in q-space imaging, data are acquired with a conventional pulsed gradient spin echo (PGSE) sequence, and the signal attenuation (E(q)) is plotted as a function of the wave-vector q (where $q = (2\pi)^{-1}\gamma g\delta$, γ being the nuclear magnetogyric ratio, g and δ are the pulse gradient strength and duration, respectively). Diffusion-diffraction phenomena occur in restricted systems with mono-disperse structure, and by measuring E(q) the compartment size can be extracted (109). However, such diffusion-

diffraction phenomena are usually not resolved in biological systems due to the size poly-dispersity (117). In such cases, the full-width at half-maximum (FWHM) of the Fourier transform of E(q) may be used to characterize the mean compartment size (69,110). Another approach using q-space imaging is the AxCaliber framework (31), which acquires multi-dimensional MRI data (q-values and diffusion times). The compartment size distribution is then estimated by modeling the intracellular diffusion using analytical expressions that are based either on the short gradient approximation (118) or on the constant diffusion gradient (119,120). In addition, a method called the angular double-PGSE has been proposed to measure small compartmental dimensions with relatively low q-values (111,112). This method usually keeps the q-value fixed but varies the orientation of the second gradient pair. The compartment dimension can be extracted from the angular dependent signal decay. However, the PGSE-based measurements usually encounter long diffusion times (> 10 ms) in practice due to gradient hardware limitations, so that the root mean square displacements (RMSD) of diffusing molecules (> 6 μm) are much larger than small axon sizes (e.g. diameter $d < 2$ μm). This in turn significantly reduces the sensitivity for detecting effects at small spatial scales. To enhance sensitivity to small scales, much higher q-values and/or more measurements with different degrees of diffusion weighting are usually necessary for PGSE measurements which in turn lead to long scan times.

The oscillating gradient spin echo (OGSE) method has been shown to be able to achieve much shorter diffusion times and hence may be able to detect smaller axons with high sensitivity (121). Moreover, the OGSE method can probe a range of effective diffusion times by tuning the oscillating gradient frequencies, and thus an apparent diffusion spectrum can be obtained which contains more comprehensive micro-structural information on biological tissues (41). For example, the OGSE method has previously been used to probe various length scales in biological systems, such as cultured cells (24), healthy rat brain (44), human brain in vivo (122,123), rat and mouse tumors (19,23,25), and brains after stroke (124). The sensitivity of the OGSE method to intracellular structure has also been investigated (21,125), and it has been shown that unique microstructure-based contrasts can be obtained which are not available from conventional PGSE experiments (28,126). Before studying quantitatively the micro-structural

properties of biological tissues, it is important to derive and validate the analytical models of OGSE as they may be used for model fitting, parameter estimation, and to optimize experiments (127). To this end, analytical expressions that predict OGSE signals in some typical structures have been derived and validated with computer simulations (128), which suggests the possibility of extracting small axon sizes using the OGSE method. However, these analytical expressions have not previously been validated or calibrated experimentally using well-characterized physical phantoms with known pore sizes.

In the current study, OGSE experiments were performed to measure the inner diameters of hollow microcapillaries with a range of sizes (~ 1.5-19.3 μm) that mimic axons in the human central nervous system (129). The fitted sizes were compared with the known values to validate the accuracy of fitting cylinder diameters using the OGSE method. In addition, the limitation of fitting free diffusion coefficients using the OGSE method was investigated. From this, a possible fast method of mapping axon size non-invasively is proposed.

Methods

Theory

The cosine-modulated OGSE waveform was chosen in the current study due to its specific diffusion spectral selectivity (18). Hence, the effective diffusion gradient is:

$$g(t) = \begin{cases} G\ cos[2\pi f t] & 0 < t < \sigma \\ -G\ cos[2\pi f(t - \Delta)] & \Delta < t < (\Delta + \sigma) \\ 0 & else \end{cases} \quad [4.1]$$

Here G is the gradient amplitude, f the diffusion gradient frequency, σ the gradient duration, Δ the separation of two diffusion gradients. The corresponding b-value is (124):

$$b = \frac{\gamma^2 G^2 \sigma}{4\pi^2 f^2} \quad [4.2]$$

Under the Gaussian phase approximation (130-133), the restricted diffusion signal attenuation can be described as (52)

$$E = exp\left(-\frac{\gamma^2}{2}\sum_k B_k \int_0^{2\tau} dt_1 \int_0^{2\tau} dt_2\, e^{-D\lambda_k|t_2-t_1|} g(t_1)g(t_2)\right) \quad [4.3]$$

where 2τ is the echo time, and B_k and λ_k are structure dependent coefficients. The analytical expressions of B_k and λ_k for some typical geometries such as parallel planes, cylinders, spheres, and spherical shells can be found in the literature (52,128). In the case of diffusion inside an impermeable cylinder with a diameter *d*,

$$B_k = \frac{(d/\mu_k)^2}{2(\mu_k{}^2-1)} \quad \text{and} \quad \lambda_k = 4(\frac{\mu_k}{d})^2 \quad [4.4]$$

where μ_k is the k^{th} root of $J_1'(\mu) = 0$ and J_1 is a Bessel function of the first kind. By substituting Eqs. [4.1] and [4.2] into Eq. [4.3] and assuming the diffusion gradient is perpendicular to the main axis of the cylinder, the measured ADC can be expressed as

$$\begin{aligned}\mathrm{ADC}(f,D,d) = 8\pi^2 \sum_k & \frac{B_k \lambda_k^2 D^2 f^2}{\sigma(\lambda_k^2 D^2 + 4\pi^2 f^2)^2} \times \\ & \left\{ \frac{\sigma(\lambda_k^2 D^2 + 4\pi^2 f^2)}{2\lambda_k D} - 1 + \exp(-\lambda_k D\sigma) + \exp(-\lambda_k D\tau)(1-\cosh(\lambda_k D\sigma)) \right\}\end{aligned} \quad [4.5]$$

where *D* is the free diffusion coefficient. Eq. [4.5] shows that ADC has a strong dependence on the gradient oscillating frequency *f*. If ADC measurements are performed at multiple gradient frequencies, the free diffusion coefficient *D* and the cylinder diameter *d* may be extracted simultaneously. This is a much different approach compared with previously reported PGSE-based models.

Experiment

All NMR diffusion experiments were performed on a Varian 7T scanner with a 12mm Doty micro-gradient coil. The maximum gradient strength used in this study was 1.88 T/m. Five different types of hollow microcapillaries (Polymicro Technologies, USA) with different inner diameters (1.5-1.6, 4.3-4.5, 9.5-9.7, 14.9-15, 19.0-19.3 μm

(lower bound–upper bound provided by the manufacturer)) and the same outer diameter around 150 μm were used as the phantoms. The microcapillaries were cut to ~ 3.5 cm in length and then immersed in distilled water for approximately two weeks. The microcapillaries were then air-dried to remove any residual water outside but retain the water inside the microcapillaries. By this means, a well-characterized one-compartment diffusion system was formed. Each type of microcapillary was packed into 5 mm NMR tubes and aligned parallel to the z-direction of the magnet. The diffusion gradients were applied perpendicular to the microcapillary main axis with a duration of 20 ms on either side of a refocusing pulse. An apodised cosine-modulated waveform which replaced the first and last quarters with half-sine lobes at double frequency was used to avoid very rapid rise times (124). Temporal diffusion spectra (41) were acquired at 12 oscillating frequencies ranging evenly from 50 Hz to 600 Hz. At each frequency, the ADC was calculated from two acquisitions with b = 0 and b = 700 s/mm^2. The only exception was for the smallest (1.5-1.6 μm) microcapillaries, in which much higher b-values were used ranging from 700 to 50000 s/mm^2 in order to cause higher diffusion weighting. Other parameters were: TR = 8 sec, TE = 60 ms, receiver bandwidth 10 kHz, spectral resolution 78.125 Hz. NEX (number of excitations) varied from 4 to 80 for different microcapillary sizes depending on the signal-to-noise ratio (SNR). The diffusion coefficient of free water was measured with distilled water in a 5 mm NMR tube at the same temperature. The same measurement was also performed with the diffusion gradient along the z-axis in the microcapillary experiments.

Data analysis

The measured ADC spectra were fit to Eq. [4.5] with two unknown variables D and d using the *lsqcurvefit* function in Matlab (Mathworks, Natick, MA). To explore the sensitivity of the ADC spectra to the cylinder diameter with a limited range of low frequencies, the ADC spectra were also fit with only a subset of frequencies (ranging from 2 to 12 in number). The fittings were processed with initial values: D = 1.8 μm^2/ms, d = 15 μm; lower bounds: D > 0 μm^2/ms, d > 0 μm; and upper bounds: D < 4 μm^2/ms, d < 200 μm.

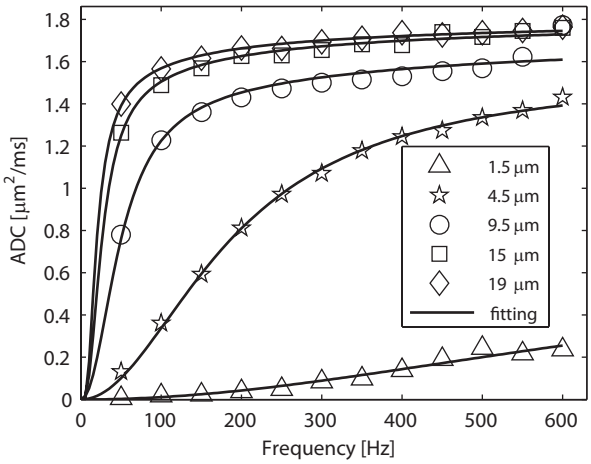

Figure 4.1 The measured ADC spectra (symbols) and fitted spectra (solid lines) for restricted diffusion inside microcapillaries with different sizes.

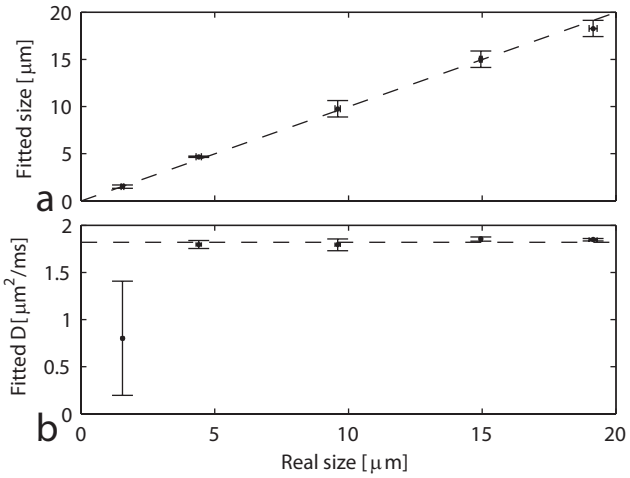

Figure 4.2 The fitted size (**a**) and the fitted free diffusion coefficient (**b**) versus the real size. The vertical error-bars represent the 95% confidence intervals of the fitted values. The horizontal error-bars represent the lower and upper bounds provided by the manufacturer. The dashed line in (**a**) is the identity line, and the dashed line in (**b**) represents the measured diffusion coefficient of free water (1.82 $\mu m^2/ms$).

Figure 4.1 shows the measured ADC spectra (markers) and fitted spectra (solid lines) with all the 12 frequencies. Consistent with the theory, the measured ADC increased with the oscillation frequency, approaching the free diffusion coefficient at higher frequencies. Note that the ADC dispersion rate with frequency was strongly

dependent on the inner diameter, implying that ADC dispersion rate alone might be a sensitive indicator of diffusion compartment size.

The comparison between the fitted microcapillary inner sizes and the sizes provided by the manufacturer is shown in Figure 4.2 (a). All microcapillary diameters were fit accurately (<6%). Note that the fitted size of the smallest microcapillaries was only -2.6% from the real value, suggesting that the OGSE method can be used to accurately measure small compartment sizes, which are usually overestimated using other methods (114,134). In addition, all fitted free diffusion coefficients are consistent with the measured diffusion coefficient of free water (1.82 $\mu m^2/ms$) except that of the smallest (1.5-1.6 μm) microcapillaries (see Figure 4.2 b), which deviates ~56% from the true value. All fitted results are summarized in Table 4.1.

Real size [μm]	Fitted size [μm]	Fitted D [$\mu m^2/ms$]
1.5-1.6	1.51±0.17	0.80±0.61
4.3-4.5	4.67±0.08	1.80±0.04
9.5-9.7	9.76±0.87	1.79±0.06
14.9-15.0	15.01±0.88	1.85±0.02
19.0-19.3	18.28±0.87	1.85±0.01

Table 4.1 Summary of the sizes and the free diffusion coefficients fitted with Eq. [4.5]. Real sizes are given by lower and upper bounds provided by the manufacturer, and all fitted values are given by mean±95% confidence intervals.

To further investigate the accuracy of the OGSE method to the smallest microcapillaries, the ADC spectrum for the 1.5-1.6 μm microcapillaries was fit using a different strategy that includes a fixed free diffusion coefficient D = 1.82 $\mu m^2/ms$ shown in Figure 4.3. The new fitted size increased to 1.75 μm but was still in reasonably good agreement with the real size. The fitted ADC spectra for the two different types of fitting were almost the same within the frequency range used in this study, although there is significant difference at higher frequencies. This is because the applied gradient frequencies for such a small size are not high enough to probe free diffusion adequately so that the ADC spectra in this low frequency range are still dominated by boundary

effects, i.e. are sensitive to restriction size. This is consistent with numerous previous reports (22,24).

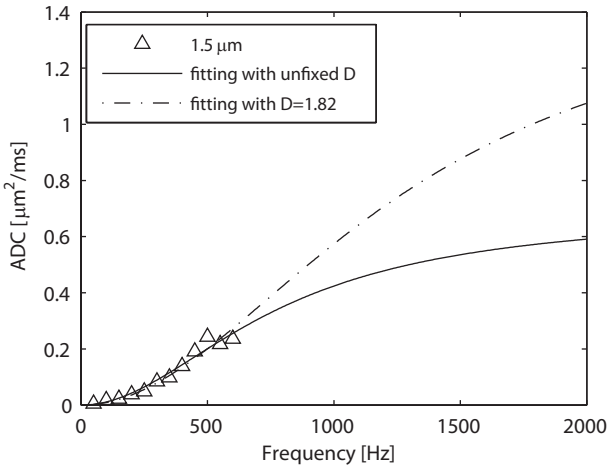

Figure 4.3 Comparison of the fitted ADC spectra for the 1.5-1.6 μm microcapillaries using two different fitting methods, i.e. with and without fixed free diffusion coefficient D = 1.82 μm^2/ms.

Figure 4.4 shows the fitted diameters using the first N (ranging from 2 to 12) frequencies. All fitted sizes were consistent with only small fluctuations regardless of the number of frequencies used in fitting. An interesting result is that a minimum of two ADC values at different frequencies is sufficient to estimate the inner diameters of hollow microcapillaries with reasonable accuracy.

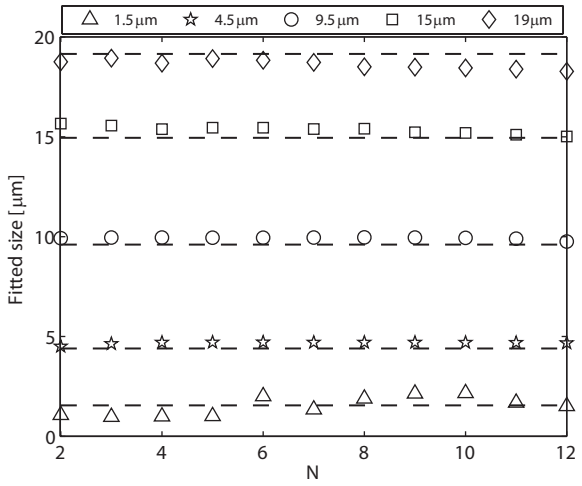

Figure 4.4 The fitted diameters against the first N frequencies used in fitting for the microcapillaries of different sizes. Dashed lines represent real values, and markers are fitted results.

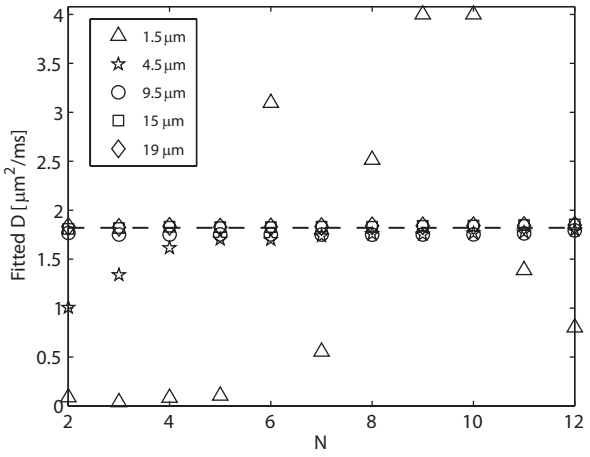

Figure 4.5 The fitted free diffusion coefficients against the first N frequencies used in fitting for the microcapillaries of different sizes. Dashed line represents the measured diffusion coefficient of free water (1.82 μm^2/ms), and markers are fitted results.

Figure 4.5 shows the fitted free diffusion coefficients using the first N (ranging from 2 to 12) frequencies. For relatively larger sizes ($d > 9.5$ μm), all the fitted free diffusion coefficients were consistent with the true values regardless of the number of frequencies used in fitting. However, the sensitivity of OGSE spectra to the free diffusion coefficient decreased with decreasing compartment sizes which could be appreciated from the 4.3-4.5 μm microcapillaries. When only the first two frequencies were used, the

fitted D was about 1.0 $\mu m^2/ms$, which was about 45% lower than the true value. However, with more and more high frequencies used in fitting, the fitted D approached quickly to the true value, indicating the free diffusion behavior is then adequately probed. By contrast, the fitted D for the smallest microcapillaries showed a remarkable fluctuation. This is due to two main reasons: (1) the applied gradient frequencies were not high enough so that the sensitivity of the OGSE measurements to free diffusion was low; and (2) the measurement SNRs of the smallest microcapillaries were about 50 and much lower than those of other microcapillaries due to significantly reduced water content (the intra-microcapillary to total space volume ratio < 0.01%). However, even if the fitted D had large errors for the smallest microcapillaries, the fitted size was still in good agreement with the real values as shown in Figure 4.4.

Discussion

The inner diameters of each sample of the hollow microcapillaries used only vary within a narrow range defined by the lower and upper bounds (135,136). Therefore, these hollow microcapillaries provide a well-characterized model system to validate the accuracy of different diffusion MRI methods (111,114-116,134). In this study, the inner diameters of hollow microcapillaries ranging from 1.5 to 19.3 μm (similar to the axon size range in the human central nervous system (129)) have been estimated accurately using the OGSE method. Note that several OGSE-like methodologies (114-116) have already been applied to detect small sizes using similar types of phantoms. To the best of our knowledge, this is the first study that validates the feasibility of using the OGSE diffusion spectra to obtain quantitative structural information in white-matter like systems. The results confirmed that the OGSE method is highly sensitive to measure small sizes non-invasively (24,30,137).

The fitting of the compartment sizes and the free diffusion coefficients is based on Eq. [4.5], which was derived based on the Gaussian phase approximation (133). The validity of the Gaussian phase approximation has been analyzed previously (119,138,139), and computer simulations have confirmed that the Gaussian phase approximation is accurate enough for most practical applications (127,128). Hence, fast ADC measurements can be performed with a few b-values, which avoid long scan times.

As shown above, when the frequencies are moderately high, the OGSE measurements can be highly sensitive to the compartment size. Even two ADC values with different frequencies may be sufficient to extract the sizes of the compartments accurately. Thus OGSE may serve as a fast measurement method for mapping axon sizes. The relatively low sensitivity of diffusion measurements in practice to the free diffusion coefficient has also been observed using the angular double-PGSE method (111). Though the free diffusion coefficient could not be extracted accurately with relatively low frequencies only, it has little influence on the extraction of the compartment sizes. The measured ADC at 50 Hz was about 1.4 $\mu m^2/ms$ for the 19-μm microcapillaries, which was 23% lower than the diffusion coefficient of free water at the same temperature. This suggests that, even if the microcapillary boundaries were not fully probed (RMSD ~ 12 μm), there was still a significant influence from the boundary restriction on the diffusion signal at such an effective diffusion time. Our results show that with the experimental parameters used in the current study the microcapillary sizes up to 19 μm can be estimated accurately. However, if microcapillaries with even larger sizes are probed with the same experimental parameters, the measured ADC may approach the free diffusion coefficient, i.e. reach the plateau of the ADC spectrum, and, hence, the microcapillary sizes will not be estimated as accurately. Compared with other methods, the OGSE method is capable of detecting small sizes around 1.5 μm accurately. The overestimation using other methods has been tentatively explained by the presence of background magnetic field gradients due to the susceptibility difference between glass and water (114,134). The OGSE sequence is intrinsically insensitive to background and imaging gradient cross terms (124,140), so it may be more suitable for extraction of axon sizes in inhomogeneous systems.

Recent analyses have suggested that the ADC measured with oscillating gradient approaches depends not only on the gradient waveforms but also on the number of oscillations (141). The number of oscillations (n) is implicitly included in Eq. (1) (note that $f = n/\sigma$). The cosine-modulated waveform has been shown to perform better than the sine-modulated waveform to fulfill the validity conditions of the high-frequency expansion of ADC (141). Our experimental settings have taken both factors explicitly into consideration so that accurate measurement results were obtained.

The implementation of OGSE methods on human scanners is challenging and limited by current gradient systems. Despite the challenge, there have been two published OGSE studies on human scanners with maximum gradient strength around 50 mT/m (122,123). Instead of the standard cosine waveforms used here, the trapezoidal gradient waveforms have been suggested and implemented to achieve higher diffusion weighting (122,123,127), though with reduced spectral selectivity. Even with frequencies < 66 Hz, ADC dispersion with frequency has already been observed in human white matter (122,123). If more powerful gradient systems are used, e.g. the Connectome gradient coils (142), much higher frequencies and b-values could be achieved in human OGSE measurements. For example, a frequency as high as 100 Hz and a b-value of 700 s/mm^2 could be possible with a gradient strength of 200 mT/m. Based on current results, the compartment sizes may be extracted in this frequency range (f < 100 Hz), which suggests that there is potential to measure axon sizes as small as 1.5 μm on human scanners using OGSE.

The current study considered only a one-compartment diffusion system which showed the feasibility of OGSE measurements for rapid measurements of small axon sizes. However, in real biological systems, there are several other confounding effects, such as the contribution from the extracellular water, the distribution of axon sizes, and the fiber orientation and dispersion (143,144). Models similar to the CHARMD model (145) but using the OGSE approach are currently under development, and are predicted to be capable of fast mapping of axon size distributions in vivo.

Conclusion

In this study, the inner diameters of hollow microcapillaries over a range of sizes (~1.5-19.3 μm) were accurately measured using the OGSE method. The accuracy of fitting cylinder diameters and free diffusion coefficients using the OGSE method was analyzed, and it suggests that OGSE measurements, even with moderately high frequencies, are highly sensitive to compartment sizes. A possible fast method of mapping axon size non-invasively is proposed.

CHAPTER V
QUANTIFICATION OF CELL SIZE USING TEMPORAL DIFFUSION SPECTROSCOPY

Abstract

Temporal diffusion spectra may be used to characterize tissue microstructure by measuring the effects of restrictions over a range of diffusion times. Oscillating gradients have been used previously to probe variations on cellular and subcellular scales, but their ability to accurately measure cell sizes larger than 10 μm is limited. In this study, a new approach has been developed to quantify cell sizes by combining measurements made using oscillating gradient spin echo (OGSE) with a conventional pulsed gradient spin echo (PGSE) acquisition at relatively long diffusion time. Based on a two-pool model (incorporating intra- and extracellular spaces), accurate estimates of cell sizes were obtained *in vitro* for different cell types with sizes ranging from 10 to 20 μm. Therefore, hybrid OGSE-PGSE acquisitions sample a larger region of temporal diffusion spectra and can accurately quantify cell sizes over a wide range.

Introduction

Cell size plays an important role in affecting the functional properties of cells from the molecular to the organismal level, such as cellular metabolism (146), proliferation (147) and tissue growth (148). For cancer diagnosis and prognosis, measurements of cell size have been widely used to differentiate cancer types (149) and monitor treatment-induced apoptosis (150). In addition to cell size, other microstructural information on a subcellular length scale, such as nuclear sizes, also provides insights into the functional properties of cancer cells. For example, nuclear size has been used to diagnose tumors (151) and distinguish low- from high-grade tumors (152). Conventionally, both cellular (e.g. cell size and cellularity) and subcellular (e.g. nuclear size and nuclear-to-cytoplasm ratio) information is obtained via invasive biopsy. However, biopsy is limited by various clinical complications, including pain, hemorrhage, infection, and even death (153). Therefore, a non-invasive technique with

the capability of detecting tissue microstructural information on both cellular and subcellular length scales would be of great interest for clinical and research applications.

Diffusion-weighted MRI (DWI) provides a non-invasive way to map the diffusion properties of tissue water molecules that are affected by restrictions and hindrances to free movement, and is thereby able to provide information on tissue microstructure. Conventionally, an effective mean diffusion rate, the apparent diffusion coefficient (ADC), is obtained by using motion-sensitizing pulsed gradient spin echo (PGSE) pulse sequences to probe water displacements. ADC values are potentially affected by various tissue properties, including cellularity (154,155), cell size (156), nuclear size (125), and membrane permeability (22). ADC values therefore reflect overall diffusion effects and are not specific for any single parameter such as cell size. More elaborate methods have also been developed to map mean compartment size in porous media or tissues. Diffusion-diffraction effects (109) have been reported to successfully characterize the mono-dispersed cell sizes of erythrocytes (157), but fail in most real biological tissues due to the heterogeneous distribution of cell sizes. Q-space imaging generates a displacement probability distribution function that can provide apparent compartment sizes in biological tissues. Unfortunately, estimates of cell size are biased in practice because of methodological limitations (for example, the short-gradient pulse approximation (158) is usually not met, and only relatively low gradient strengths are available on regular MRI systems (110)) and the inherent complexity of real biological tissues (e.g. the existence of multiple compartments (110) and coexisting inflammation (159)). To overcome these problems, multi-compartment models that mimic real tissues have been developed to more accurately characterize cell size. For example, models that include more than one compartment and/or the effects of membrane permeability have been used to assess axon sizes in bovine optic nerve (160), to characterize axon size distributions *in vitro* (31) and *in vivo* (161), and to quantify mean axon size in the corpus callosum of human (162) and monkey brain (163). In addition, as an extension of the PGSE method, the double-PGSE sequence has been used to measure cell size and anisotropy in fixed yeast cells (164). However, despite these successes, subcellular microstructural information has not been obtainable by practical PGSE-based methods. One reason is that PGSE sequences typically employ a diffusion time of 20-80 ms *in vivo*

due to hardware limitations. Thus, the characteristic diffusion length probed by water molecules is on the order of 5-20 μm, which is similar to the distance between hindering cell membranes of typical eukaryotic cells. As a result, PGSE measurements are sensitive to cellularity in biological tissues, but cannot isolate the effects of subcellular structures (< 5 μm). Consequently, conventional PGSE methods are suited to characterize cell sizes and cell densities in biological tissues non-invasively, but do not in practice provide information on subcellular microstructure.

Oscillating gradient spin echo (OGSE) sequences have emerged as a novel means to obtain much shorter effective diffusion times by replacing bipolar diffusion-sensitizing gradients in PGSE methods with oscillating gradients (121,165,166). Previous reports have shown that OGSE measurements, even at moderately low frequencies, are capable of detecting restrictions to water diffusion over a short spatial scale (< 5 μm) which is usually not accessible by conventional PGSE methods (165). Moreover, by varying the oscillation frequency (f), temporal diffusion spectra can be obtained to provide more comprehensive information about biological tissues at both cellular and subcellular length scales (23,24). OGSE sequences have been successfully implemented and used to measure abnormal brain metabolites (167) and treatment-induced variations in organelles (73), nuclear size changes after anti-cancer therapy (168) and hypoxia-ischemia (27,42). Recently, there has been increasing interest in using OGSE methods to measure axon sizes (34,116,169). However, despite these successes in probing microstructure, the ability of OGSE sequences that use harmonic waveforms to probe relatively large cell sizes is, ironically, limited by the maximum achievable diffusion time within the constraints of practical echo times. In typical cosine-modulated OGSE methods, the effective diffusion time $\Delta_{diff} = 1/(4f) = \delta/(4N)$, where f is the frequency, δ is the duration of diffusion gradient, and N is the number of oscillations in each gradient (165). Hence, even for a very long gradient duration of 100 ms, the maximum achievable Δ_{diff} = 25 ms, corresponding to a diffusion distance ≈ 10 μm if the diffusion coefficient is 2 $\mu m^2/ms$. Such a relatively short displacement significantly decreases the ability to quantify larger cell sizes (e.g. 10 – 20 μm), which is typical in tumors. Moreover, long gradient durations and lower frequencies in practice may not be used because of signal losses caused by T_2 relaxation. As an example, as shown in our recent histology-validated measurements

using OGSE to measure mean axon diameters, dimensions in the range 1 to 5 μm were measured accurately, but the axon diameters larger than 6 μm were significantly underestimated (34).

For a general time-dependent gradient, the diffusion-weighted MR signal can be expressed as (165)

$$S = S_0 \exp\left[-\frac{1}{\pi}\int_0^\infty \mathbf{F}(\omega)\mathbf{D}(\omega)\mathbf{F}(-\omega)d\omega\right], \quad [5.1]$$

where $\mathbf{F}(\omega)$ is the Fourier transform of the time integral of the diffusion gradient, and $\mathbf{D}(\omega)$ is the frequency-dependent diffusion tensor that contains microstructural information. With appropriately designed gradient waveform (e.g. cosine-modulated), $\mathbf{F}(\omega)$ can serve as a well-defined sampling function and hence $\mathbf{D}(\omega)$, the temporal diffusion spectrum, can be obtained. However, due to hardware limitations, it is impossible to achieve all frequencies in practice, and hence only a segment of a diffusion spectrum can be acquired. For a conventional PGSE sequence, in which δ is the gradient pulse width and Δ is the diffusion time, $|F(\omega,\Delta)| = \gamma\delta\Delta G \frac{\sin(\omega\delta/2)\sin(\omega\Delta/2)}{(\omega\delta/2)(\omega\Delta/2)}$, which therefore samples low frequency regions of the spectrum that are difficult to sample with oscillating waveforms. In Figure 5.1, the spectrum is divided into two regions by the grey band, representing the readily accessible spectral ranges for PGSE (left) and OGSE (right) methods, separately. For the diffusion spectra of restricted water diffusion inside impermeable spheres (Figure 5.1), the rise in apparent diffusion coefficient in response to an increase in the frequency is the key to extract cell size (34). In order to measure the size of spheres smaller than 10 μm, an appropriate observation window can be chosen in the OGSE-accessible region to capture the rising portion of the curve. However, as the cell size becomes larger, the spectra in the right region are almost flat and the observation window needs to extend to the PGSE-accessible region. In the current study, 40 and 80 Hz OGSE measurements and PGSE with a diffusion time of 52 ms (labeled by vertical dash line in Figure 5.1) were combined, corresponding to an observation window with Δ_{diff} from 3.13 to 52 ms. We hypothesized that such a combination would cover a broader segment of the temporal diffusion spectrum and enable the quantification of larger cell

sizes (up to 20 μm). In the rest of the paper, this hypothesis is elucidated and validated using both computer simulations and well-characterized cell culture experiments.

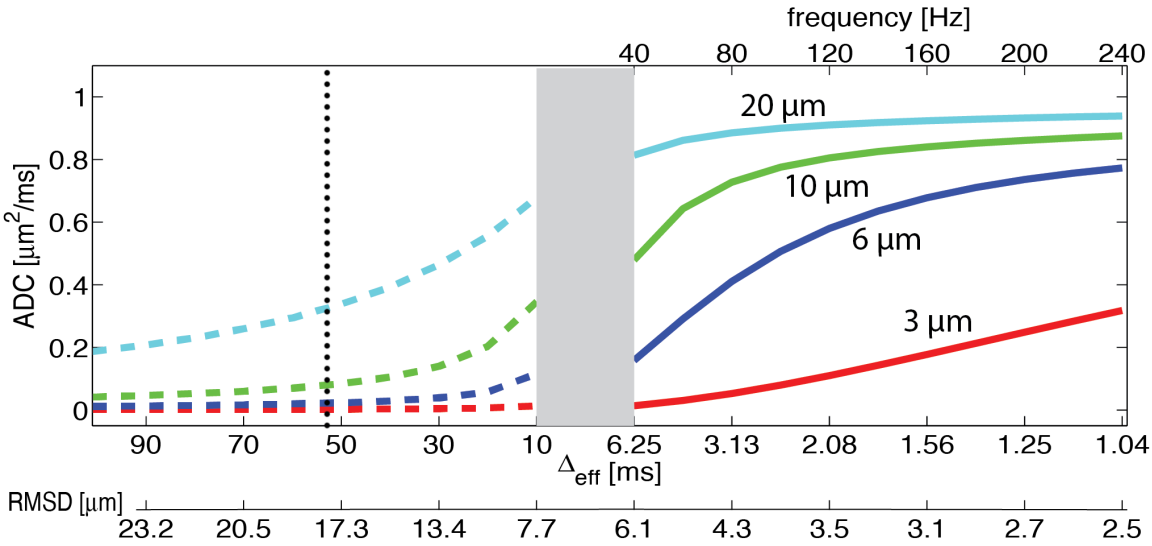

Figure 5.1 Diffusion spectra of restricted water diffusion inside impermeable spheres with diameters of 3, 6, 10, and 20 μm. The grey band divides the spectrum into two regions, representing the readily accessible spectral ranges for PGSE (left) and OGSE (right) methods, separately.

Methods

We assume that the diffusion-weighted signals of cell samples can be expressed as the sum of signals arising from intra- and extracellular spaces, namely,

$$S = f_{in} \cdot S_{in} + (1 - f_{in}) \cdot S_{ex}, \qquad [5.2]$$

where f_{in} is the water volume fraction of intracellular space, and S_{in} and S_{ex} are the signal magnitudes per volume from the intra- and extracellular spaces, respectively. The water exchange between intra- and extracellular spaces is omitted, as suggested in the CHARMED model (170).

Cells are modeled as spheres despite the significant variations of cell shape in realistic tissues. The analytical expressions of OGSE signals in some typical geometrical structures, e.g. cylinders and spheres, have been derived previously (47). For OGSE measurements of diffusion within impermeable spheres using cosine-modulated gradient waveforms, the intracellular diffusion signal can be expressed as

$$S_{in}(OGSE)=\exp\Big(-2\gamma^2g^2\sum\nolimits_n\frac{B_n\lambda_n^2D_{in}^2}{(\lambda_n^2D_{in}^2+4\pi^2f^2)^2}\Big\{\ \frac{\lambda_n^2D_{in}^2+4\pi^2f^2}{\lambda_nD_{in}}\Big[\frac{\delta}{2}+\frac{\sin(4\pi f\delta)}{8\pi f}\Big]$$
$$-1+\exp(-\lambda_nD_{in}\delta)+\exp(-\lambda_nD_{in}\Delta)(1-\cosh(\lambda_nD_{in}\delta))\Big\}\Big) \quad [5.3]$$

where D_{in} is the intracellular diffusion coefficient, f is the oscillation frequency, δ is the gradient duration, Δ is the separation of two diffusion gradients, λ_n, B_n are structure dependent parameters containing sphere diameter. The accuracy of Eq. [5.3] has been validated by computer simulations (47) and phantom experiments (49). Note that, if $f\to 0$, a cosine-modulated OGSE pulse degenerates into a conventional PGSE pulse and hence Eq. [5.3] becomes

$$S_{in}(PGSE)=\exp\Big(-2\frac{\gamma^2g^2}{D_{in}^2}\sum\nolimits_n\frac{B_n}{\lambda_n^2}\big\{\lambda_nD_{in}\delta-1$$
$$+\exp(-\lambda_nD_{in}\delta)+\exp(-\lambda_nD_{in}\Delta)(1-\cosh(\lambda_nD_{in}\delta))\big\}\Big) \quad [5.4]$$

Therefore, Eqs. [5.3] and [5.4] describe intracellular diffusion signals obtained using OGSE and PGSE methods, respectively, and the microstructural parameters (i.e. λ_n and B_n, as well as sphere diameter) can be fit simultaneously using these equations.

Currently, only a narrow range of frequencies (less than 160 Hz) may be sampled with clinically achievable gradient strengths (< 15 G/cm). Under such circumstances, the ADC values for the extracellular space have been reported to show a linear dependence on the oscillating-gradient frequency (34). As a result, the extracellular diffusion signal can be modeled as a linear function of gradient frequency, namely,

$$S_{ex}(OGSE)=\exp[-b(D_{ex0}+\beta_{ex}\bullet f)] \quad [5.5]$$

where D_{ex0} is a constant and β_{ex} is the slope of extracellular diffusion coefficient with respect to frequency f, which contains information on structural dimensions but may not be simply assigned to any specific morphological feature in the tissue. If $f\to 0$, a cosine-modulated OGSE pulse degenerates into a conventional PGSE pulse and Eq. [5.5] becomes:

$$S_{ex}(PGSE)=\exp[-bD_{ex0}] \quad [5.6]$$

Biological tissue was modeled as a two-compartment system, consisting of intracellular and extracellular spaces, without any water exchange between these two compartments. Cells were modeled as a collection of densely packed spheres on a face-

centered cube (FCC) (125). The following diffusion and morphological parameters were used in the simulation: D_{in}= 1 μm^2/ms, D_{ex}= 2 μm^2/ms, cell diameter = 2.5, 5, 10, 15, 20, and 25 μm, intra-cellular volume fraction = 43%, 51%, and 62%. A finite difference method was employed, and further details of the computational aspects of the simulations have been reported elsewhere (53). Diffusion-weighted signals were simulated for both OGSE and PGSE sequences with the same parameters set in the cell culture experiments.

Two sets of cell experiments, designated as "A" and "B", were performed. Experiment "A" was designed to measure cell sizes for different types of cells at different densities, while experiment "B" was designed to characterize the changes in the tumor cell size before and after anti-cancer treatment. In experiment "A", murine erythroleukemia (MEL) and human promyelocytic leukemia K562 cells, purchased from American Type Culture Collection (ATCC, Manassas, VA), were cultured in DMEM medium supplemented with 10% FBS, 50 U/ml penicillin, and 50 μg/ml streptomycin (Invitrogen, CA) under standard culture conditions in a humidified incubator maintained at 5% CO_2 and 37 °C. Cells were spread every three days by 1:10 dilution and cell density was limited to be no more than 0.8 $\times 10^6$ cells/ml. All cell samples were collected, washed with PBS, and then fixed with 4% paraformaldehyde in PBS for over 2 hours. After fixation, cells were washed, and transferred to a 0.65ml Eppendorf tube. In order to obtain different cell densities, tubes were divided into three groups and centrifuged (Bio-rad microcentrifuge) at three different centrifugal forces (200, 1000, and 6000 g) for 2 minutes to result in three different cell densities. The liquid on the top was carefully removed, and the residual cell pellets, whose net weights were around 150 to 200 mg, were used for NMR measurements.

In experiment "B", nab-paclitaxel (Abraxane) treated MDA-MBA-231 cells were used to mimic the effects of anti-cancer therapy on cell sizes. Abraxane is an FDA-approved mitotic inhibitor drug used in the treatment of breast, lung and pancreatic cancers (43, 44). It interrupts cell division during the mitotic (M) phase of the cell cycle when two sets of fully formed chromosomes are supposed to separate into daughter cells. Cells are thereby trapped in the M phase and then undergo apoptosis. Note that cells significantly increase their sizes during the M phase, and hence the cell size can be used a surrogate biomarker to monitor the efficacy of Abraxane treatment. Human breast cancer

cells MDA-MBA-231 are highly metastatic and show a positive response to Abraxane treatment. MDA-MB-231 cells were cultured in the same way as MEL and K562 cells. After that, a half of the MDA-MB-231 cells were treated with 200nM of Abraxane for 24 hours. All cell samples were collected, washed with PBS, and then fixed with 4% paraformaldehyde in PBS for over 2 hours. After fixation, cells were washed, and transferred to a 0.65ml Eppendorf tube. Tubes were centrifuged (Bio-rad microcentrifuge) at 1000g for 2 minutes.

All measurements were performed on a 7.0-T, 16-cm bore Varian DirectDrive™ spectrometer (Varian Inc. Palo alto, CA). As described in 'cell preparation' section, MEL and K562 cells were prepared at three different cell densities (low, medium and high) with 4 samples at each density. Nine b-values evenly distributed between 0 and 2000 s/mm^2 were used in both PGSE and OGSE measurements. The OGSE pulse sequence substitutes the two bipolar diffusion-sensitizing gradients in PGSE with two apodized cosine-modulated gradients. Details of the OGSE pulse sequence can be found in (124). For PGSE experiments, diffusion gradient durations were δ=4 ms, and separation Δ=52 ms. The OGSE method measured frequencies at 40, 80, and 120 Hz with δ/Δ=25/30 ms. Note that the echo times (TE=60 ms) for both PGSE and OGSE measurements were the same to minimize relaxation effects.

The PGSE and OGSE diffusion signals were fit to Eq. (1)-(5) with five unknown variables: cell diameter d, intracellular diffusion coefficient D_{in}, intracellular volume fraction f_{in}, and extracellular parameters D_{ex0} and β_{ex} (see Eq.(5)), using the lsqcurvefit function in Matlab (Mathworks, Natick, MA). The constraints for fitting parameters were: $0 \le d \le 40$ μm, $0 \le f_{in} \le 1$, $0 \le D_{in} \le 3.0$ μm^2/ms, $0 \le D_{ex0} \le 3.0$ μm^2/ms, and $0 \le \beta_{ex} \le 2$ μm^2. Randomly-generated initial parameters values were used. To ensure the global minimum was reached, the fitting was repeated 100 times for each sample, and the analyses corresponding to the smallest fitting residual were chosen as the final results.

The correlations between fitted and preset intracellular volume fractions was assessed using Kendall's tau correlation coefficient (171). The differences in MR-derived cell sizes and intracellular volume fractions among the cell samples having different densities (Figure 5) were summarized using means and standard deviations, and compared by one-way ANOVA. The differences in the other three fitted parameters (D_{in},

D_{ex0}, and β_{ex}) among the cell samples having different densities (Figure 6) were summarized using means and standard deviations, and compared by one-way ANOVA. All the tests were two-sided and a p-value of 0.05 or less was taken to indicate statistical significance. Statistical analyses were performed using OriginPro 9.0 (OriginLab. Northampton, MA).

Results

For model systems mimicking tightly packed cells of diameter ranging from 2.5 to 25 μm and various intracellular volumes (43%, 51%, and 62%), both the OGSE signals with frequencies ranging from 40 to 160 Hz and the PGSE signals with a single long diffusion time of 48 ms were obtained from simulations. The size and intracellular volume fraction were fitted from three different combinations of the simulated data, including OGSE at 40 and 80 Hz, OGSE at 40 and 80 Hz + PGSE, and OGSE at 40, 80, 120, and 160 Hz. The cutoff frequencies, 80 and 160 Hz, are determined by two different maximum gradient strengths, 15 and 40 G/cm, corresponding to readily achievable gradient strengths on regular animal scanners and those with advanced human gradient coils (172), respectively. Figure 5.2 (A) shows the fitted mean sizes of cells at three different densities. The OGSE method employing a maximum gradient strength of 15 G/cm is sufficient to extract the sizes of the cells smaller than 8 μm, while it underestimates the sizes of the cells larger than 8 μm. For cells larger than 8 μm, the accuracy of size measurement can be significantly improved by incorporating either PGSE or more OGSE data with more frequencies. Correlations between fitted and preset intracellular volume fractions are shown in Figure 5.2 (B) and were measured *via* Kendall's concordance coefficient. The calculated value of Kendall's coefficient was 0.6 ($p=0.0007$), 0.75 ($p<0.0001$), and 0.72 ($p<0.0001$) for OGSE at 40 and 80 Hz, OGSE at 40 and 80 Hz + PGSE, and OGSE at 40, 80, 120, and 160 Hz, respectively. The fact that our proposed combination has a strong correlation demonstrates that this approach is a useful tool for the quantification of the intracellular volume fraction.

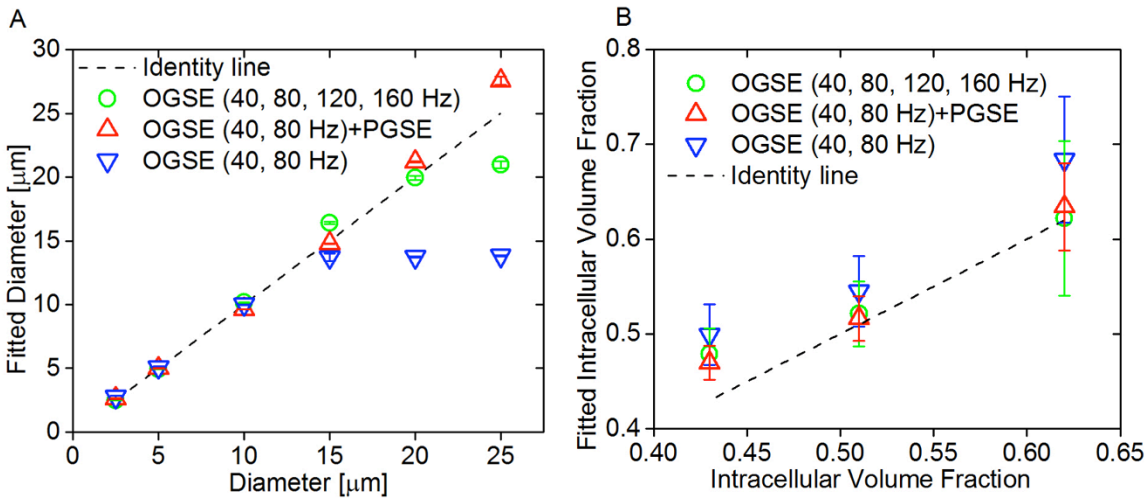

Figure 5.2 (A) Correlation between fitted diameters and preset diameters in simulations. Fitted diameters generated from three different combinations of OGSE and PGSE signals, mean ± std (n=3, with three different intracellular volume fractions: 43%, 51%, and 62%) vs. preset diameters. The dot line represents the identity line. (B) Fitted intracellular volume fraction generated from three different combinations of OGSE and PGSE signals, mean ± std (n=6, with cell size ranging from 2.5 to 25 μm) vs. preset intracellular volume fractions. The dot line represents the identity line.

Representative OGSE and PGSE signals for a sample K562 cell pellet with medium density are shown in Figure 5.3. As expected, the diffusion-weighted signals decay faster as the effective diffusion time decreases. The PGSE signals were significantly higher than OGSE signals, indicating that lower effective diffusion rates were obtained at longer diffusion times. The solid lines represent the fits from Eq. [5.1].

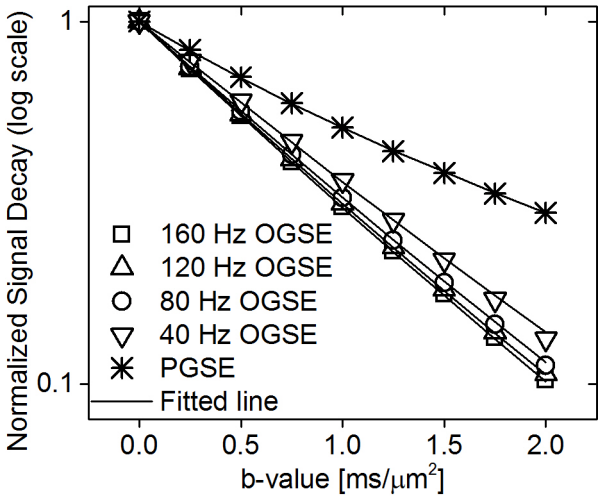

Figure 5.3 Typical OGSE and PGSE signals for the K562 cell pellet which was centrifuged at a centrifugal force of 1000g. The solid line represents the fit using Eqs. [5.1-5.5].

Figure 5.4 shows typical 40x microscope images for K562 (top) and MEL (bottom) cells. It is evident that K562 cells are much larger than MEL cells. The area of each cell was calculated from these light microscope images using an auto-segmentation program written in Matlab, and then converted to a diameter assuming each cell is a sphere. The area-weighted diameters (24) for K562 and MEL, which were determined from approximate 1000 cells, were 20.94±1.08 and 11.74±1.30 μm, respectively.

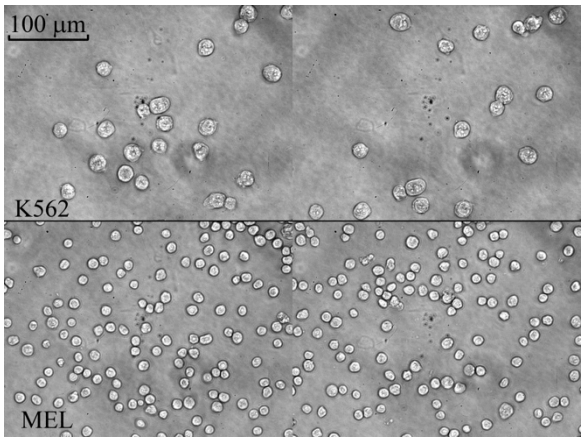

Figure 5.4 Typical 40x light microscopy pictures for K562 (top) and MEL (bottom) cells.

Figure 5.5 compares the diameters (A) and intracellular volume fractions (B) fitted from three combinations of diffusion-weighted signals for K562 and MEL cells at

three different densities. The two parameters extracted from 40 and 80 Hz OGSE signals have dramatic variations among the samples having the same cell types and the same densities, indicating that the combination of 40 and 80 Hz OGSE signals does not generate reliable results under these experimental conditions.

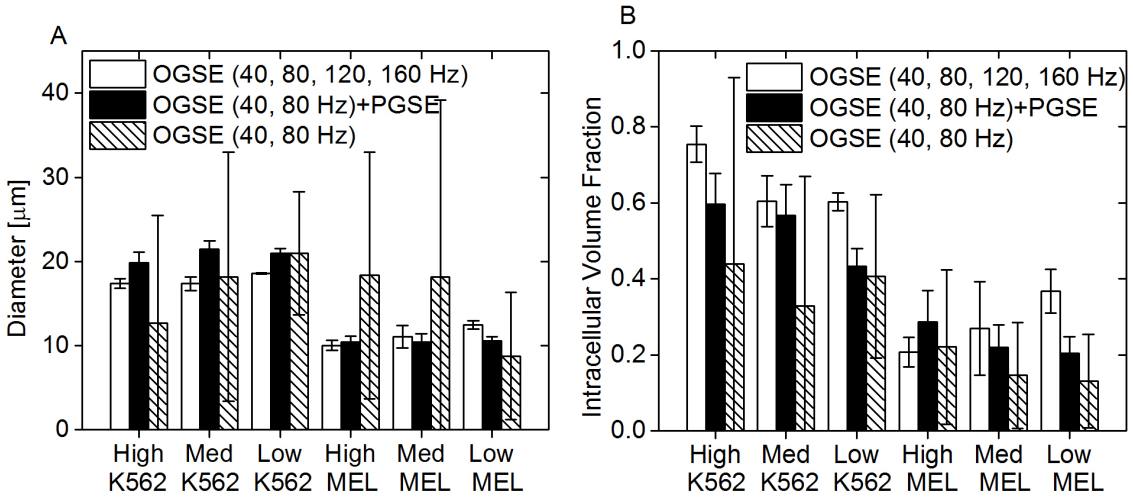

Figure 5.5 Diameter (left) and intracellular volume fractions (right) fitted from three combinations of OGSE and PGSE signals for K562 and MEL cells at three different densities: high, medium, and low. It is noted that varying cell density does not affect the fitted cell size for the same type of cells regardless of the data combination ($p>0.05$).

Using the high-frequency OGSE data, the mean diameters for K562 and MEL cells at three densities are close to the microscope-derived diameters. However, one-way ANOVA revealed that the diameters for the samples at low density are significantly larger than those from the high ($p= 0.04$ and 0.005 for K562 and MEL, respectively) and medium densities ($p= 0.03$ and 0.04 for K562 and MEL, respectively). Similarly, the mean intracellular volume fractions for MEL cells at high density are significantly lower than those for the low density ($p=0.004$), suggesting that this combination of OGSE signals does not estimate the intracellular volume fraction reliably.

	Density			Light microscope
	high	medium	low	
K562	19.82±1.30	21.5±0.98	20.96±0.60	20.94±1.08
MEL	10.42±0.72	10.46±0.98	10.6±0.48	11.74±1.30

Table 5.1 Fitted and microscope-derived diameters for K562 and MEL cells at different cell densities (low, medium, and high).

By contrast, by combining the PGSE and low-frequency OGSE signals, the fitted cell sizes are not only consistent with microscope-derived sizes (Table 5.1) but also insensitive to the variations in cell density ($p>0.05$), indicating this approach is accurate for size quantification and robust to varying cell densities. Moreover, the intracellular volume fractions for cell samples of high density are significantly higher than that for low-density samples ($p=0.02$ and 0.03 for K562 and MEL, respectively). The medium-density samples were not differentiated from the other two densities ($p>0.05$).

In Figure 5.6, the other three parameters (D_{in}, D_{ex0}, and β_{ex}) obtained from the combination of PGSE and low-frequency OGSE signals are displayed. D_{in} remains almost constant for different cell densities and cell types. D_{ex0} increases with the decreasing cell density ($p<0.05$), possibly because of the increased extracellular tortuosity. β_{ex} does not show any apparent correlation with the cell density ($p>0.05$).

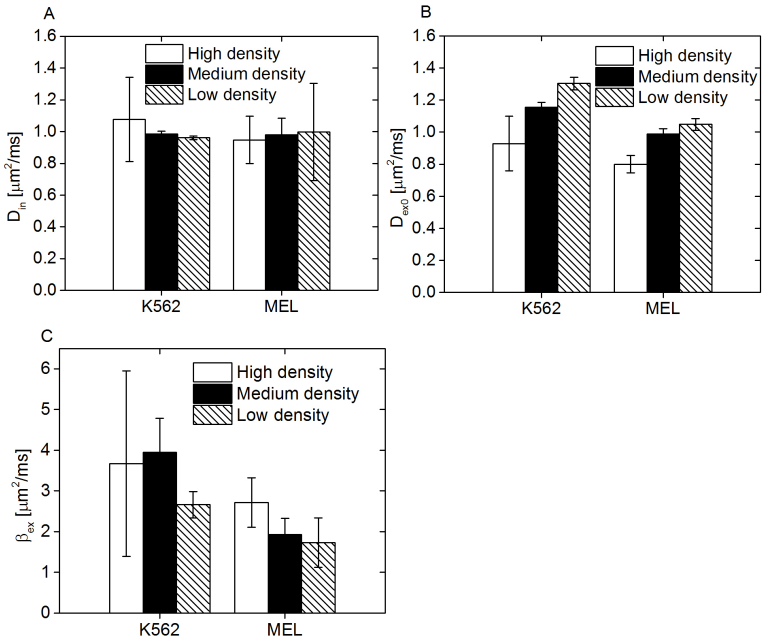

Figure 5.6 Fitted D_{in}, D_{ex0}, and β_{ex} for K562 and MEL cells at different cell densities: low, medium, and high.

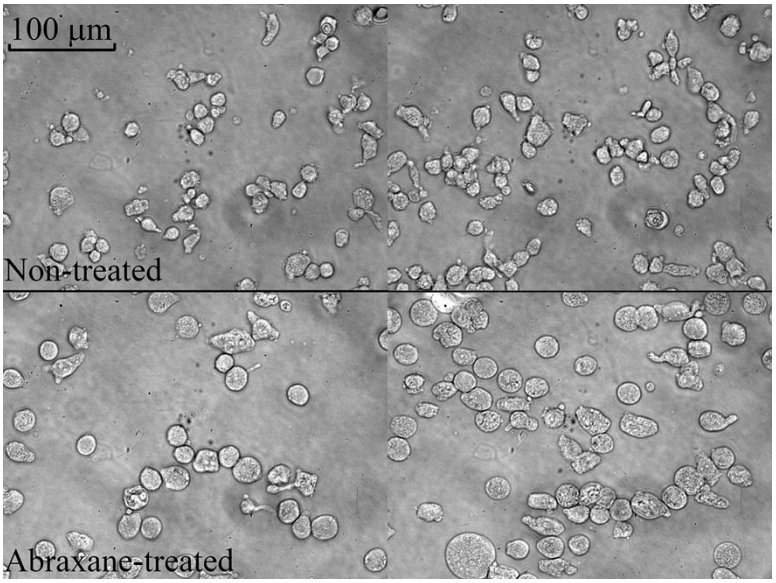

Figure 5.7 Typical 40x light microscopy pictures for non-treated (top) and Abraxane-treated (bottom) MDA-MBA-231 cells.

Abraxane is used to trap cells in the M phase and then undergo apoptosis. It is known that cells significantly increase their sizes during the M phase. Our microscope observations (Figure 5.7) confirm that Abraxane-treated cells are larger on average than the untreated MDA-MBA-231 cells. MRI-derived cell sizes are close to the area-weighted diameters calculated from light microscopy (Table 5.2), indicating that the proposed approach is capable of quantifying increases in cell sizes in response to anti-cancer treatment. Table 5.3 shows the other four parameters (D_{in}, f_{in}, D_{ex0}, and β_{ex}) for Abraxane-treated and non-treated cells. The intracellular volume fraction became larger after treatment most likely due to the increase of individual cell size, although the packing density for large cells was lower than small cells. The extracellular diffusion coefficient (D_{ex0}) increased in the cell samples with larger cells, presumably due to the increased mean restricting distances in the extracellular spaces. Note that the changes of D_{in} may not reflect the true values because the applied gradient frequencies were not high enough to sensitize the intracellular free diffusion (49).

	Fitted	Light microscope
Non-treated	14.9±1.58	15.72±1.84
Abraxane-treated	22.24±0.36	22.48±0.9

Table 5.2 Fitted and microscope-derived diameters for nontreated and Abraxane-treated MDA-MB-231 cells.

	D_{in} (μm^2/ms)	Intracellular volume fraction (%)	D_{ex0} (μm^2/ms)	β_{ex} (1000*μm^2)
Non-treated	0.62±0.018	42±6.8	0.84±0.047	4.2±0.39
Abraxane-treated	0.76±0.0012	59±2.3	1.00±0.029	4.17±0.87

Table 5.3 Fitted D_{in}, intracellular volume fraction, D_{ex0}, and β_{ex} for MDA-MB-231 cells.

Discussion

Various microstructural features of tumors, such as the cellularity, cell size, and nuclear size, play an important role in the diagnosis and prognosis of cancer. Conventionally, these parameters are obtainable only from invasive biopsy. Diffusion-weighted MRI provides a means to probe cellular characteristics of biological tissues non-invasively, and hence is potentially a viable approach for non-invasively obtaining critical information about cancer. Although PGSE and OGSE sequences are often conceived of as different, the theory of temporal diffusion spectroscopy shows how the information obtainable from different sequences is related. While OGSE implementation allow probing of the high frequency regions of a diffusion spectrum, PGSE has some advantages in practice for assessing low frequency values of the spectrum, a region that appears critical for accurately estimating the sizes of larger scale structures. PGSE methods are sensitive to cell size and cellularity, but relatively insensitive to subcellular microstructures. By contrast, OGSE methods are more sensitive to features that restrict diffusion at a subcellular scale, such as nuclear size, but in practice are not well suited to measuring larger structures. Our PGSE measurements with a single long diffusion time (52 ms) sample the diffusion spectra close to $f \to 0$, extending the range of OGSE spectral data. By sampling a sufficient range of frequencies, a larger range of cell sizes (6 – 20 μm) can be accurately measured. This combination extends the ability of diffusion measurements to probe microstructural parameters over a broader range of length scales, from subcellular scales to large cell sizes. This more comprehensive information may have significant potential in cancer imaging.

Although it is possible to implement both conventional PGSE or OGSE methods to characterize cell dimensions and subcellular scales, respectively, this strategy is time-consuming and hence impractical in clinics. Previous studies have reported one hour scanning for PGSE-based methods to obtain mean axon diameter of human corpus callosum (162) and 2.5 hours to obtain the mean cell size of mouse tumors (32). Multi-frequency and multi-b-value OGSE measurements are also time-consuming especially with a limited signal-to-noise ratio (SNR) (34). In the current study, we report a novel approach to combine OGSE and PGSE measurements with a single, long diffusion time. Such an approach significantly improves the ability of OGSE methods to accurately

measure large cell size (up to 20 μm) with slightly increased scanning time. Therefore, both cellular and subcellular information can be obtained by such an approach in limited scanning time, which may be of crucial interest in practice.

Both the simulations and cell culture experiments demonstrate that the temporal diffusion data obtained with combined PGSE and OGSE measurements enable an accurate *in vitro* estimation of cell size ranging from 10-20 μm using a maximum gradient strength of 15 G/cm. This gradient strength is available with the recently developed Connectome gradient coil, which provides a gradient strength up to 30 G/cm for human heads. Even for normal gradient coils with relatively low gradient strength, e.g. < 8 G/cm per channel, on regular MRI machines, it is still possible to employ our method. For example, a gradient duration δ = 25 ms was used in this work. Since the b value is proportional to δ^3 and G^2, a gradient strength of 7.5 G/cm can result in the same b values used in the current study with δ = 40 ms, a typical gradient duration for human OGSE studies (43,173). This means that our proposed approach is directly translatable to current human imaging, although it will benefit significantly from more advanced gradient coils.

It is also shown that incorporating more high-frequency OGSE data improves the accuracy of cell size estimates for large cells. The high-frequency OGSE data are considered to have higher sensitivity to detect small dimensions, so it is interesting that they helped make the measurements of larger cell sizes more accurate. As discussed previously, the rise in apparent diffusion coefficient in response to an increase in the frequency is the key to extract cell size (34). As shown in the curves with 10 – 20 μm in Figure 5.1, ADCs kept increasing at 120 and 160 Hz, indicating that these OGSE frequencies are still sensitize to large cell size ranging from 10 to 20 μm. When more and more frequencies that sensitize the cell size were included in the cell size fitting, more accurate results were obtained even if those relatively higher frequencies had lower sensitivities to large cell size. However, this broader frequency range method shows larger errors compared with our approach in measuring large cell size. For example, as shown in figure 5.5 (A), our approach led to 5.34%, 2.67%, and 0.08% deviations from the microscopy-derived diameters for K562 cells at high, medium, and low densities, respectively, while the broader frequency method led to deviations of 16.97%, 17.16%

and 11.36%. More importantly, the acquisitions of high-frequency OGSE data covering the same range of b-value need very high gradient strength (40 G/cm), which limits the clinical use of this approach.

The water exchange between intra and extracellular spaces was assumed negligible in the current study. This assumption has been used in previous OGSE studies (23,168,174), because the effective diffusion time of the OGSE measurement is usually much shorter (< 5 ms) compared with the intracellular lifetime of water molecules (79,175). However, the precise effect of water exchange on diffusion measurements *in vivo* remains unclear. The incorporation of PGSE measurements with a long diffusion time makes this method more likely to be affected by water exchange than typical OGSE methods. In addition, membranes of tumor cells may have altered permeability resulting from either treatment or tumor development (84). Therefore, the influence of water exchange effects on the proposed approach needs to be further investigated, especially for *in vivo* studies. A more complex model which can account for water exchange between intra and extracellular spaces, such as the Karger model (176), will be investigated in a future study.

The current study used a simplified model which describes cells as homogenous spheres without nuclei. Interestingly, cell sizes fitted by this sphere model are reasonably accurate for non-spherical MDA-MBA-231 cells (Figure 5.7), suggesting that this method may not be very sensitive to variations in cell shape. This is encouraging since cells in real biological tissues are usually not spherical. On the other hand, it has been found in computer simulations and *in vivo* studies that a change of nuclear size can affect high-frequency OGSE signals (23,125). A change of nuclear size is widely observed in many biological processes, such as necrosis and apoptosis induced by cancer treatment. Therefore, it will be valuable to develop a more comprehensive model and broader range of measurements to be able to quantitatively characterize cell size, cell density, and nuclear size. If successful, this could provide more quantitative tissue characterization of tumors.

Fitted intracellular volume fractions also show a good correlation with cell densities. However, it is technically demanding to perform the histology validation for in vitro cell pellets. As an alternative, it has been reported that the intracellular volume

fraction can be extracted from changes of diffusion-weighted signal in the extracellular space, resulting from the administration of Gadolinium-based contrast agent which changes the T1 of the extracellular space only (84). Efforts to compare intracellular volume fractions generated from these two methods are in progress.

Conclusion

Temporal diffusion spectroscopy combining a single long diffusion time PGSE and low-frequency OGSE measurements, was developed for accurately measuring relatively large cell sizes (10-20 μm). Using this method, accurate cellular sizes were obtained with a weak gradient strength of 15 G/cm, in different cancer cells and at three different cell densities. Size changes in breast cancer cells MDA-MBA-231 in response to chemotherapy were also detected. These findings were confirmed by light microscopy and confirm the potential of this method for providing microstructural information non-invasively to assist better diagnosis and prognosis of cancer.

CHAPTER VI
SUMMARY AND FUTURE DIRECTION

In chapter 2, we studied the relation between the changing rate of ADC with frequency (Δ_fADC) and the cylinder radius (R). Δ_fADC is not a monotonic function of R, and becomes larger when the cylinder radius R is close to the corresponding root mean square displacement (RMSD) at the applied oscillating frequency. The frequency (f_0) at which Δ_fADC reaches its maximum is then an essential feature of ADC spectra that correlates with intrinsic tissue structure. It suggests that measuring ADC spectra at multiple diffusion frequencies/times around f_0 is key to obtaining structural dimensions from diffusion measurements. From this, we proposed to combine OGSE and PGSE measurements in order to cover a broad range of effective diffusion times and be sensitive to a wide range of restricting dimensions.

It should be noted that quantification of cell size *in vivo* would be much more challenging than that *in vitro*. First, in biological tissues with tightly packed cells, the cell shape is irregular and the size distribution can be broad. The simple two-pool model may not be suitable for the complex situations. Second, the water exchange effects may not be negligible for *in vivo* applications. Though OGSE measurements are usually not affected by permeability changes, permeability may have a significant influence on PGSE measurements, which in turn would affect the proposed hybrid OGSE-PGSE method. Therefore, the influence of water exchange effects on the proposed approach and the quantification of cell size *in vivo* with improved model will be further investigated in future studies.

REFERENCES

1. Gerlach W, Stern O. Das magnetische moment des silberatoms. Zeitschrift für Physik A Hadrons and Nuclei 1922;9(1):353-355.
2. Frisch R, Stern O. Über die magnetische Ablenkung von Wasserstoffmolekülen und das magnetische Moment des Protons. I. Zeitschrift für Physik 1933;85(1-2):4-16.
3. Rabi I, Millman S, Kusch P, Zacharias J. The Molecular Beam Resonance Method for Measuring Nuclear Magnetic Moments. The Magnetic Moments of Li 6 3, Li 7 3 and F 19 9. Physical review 1939;55(6):526.
4. Rabi II. Space quantization in a gyrating magnetic field. Physical Review 1937;51(8):652.
5. Purcell EM, Torrey H, Pound RV. Resonance absorption by nuclear magnetic moments in a solid. Physical review 1946;69(1-2):37.
6. Bloch F. Nuclear induction. Physical review 1946;70(7-8):460.
7. Lauterbur PC. Image formation by induced local interactions: examples employing nuclear magnetic resonance. Nature 1973;242(5394):190-191.
8. Mansfield P, Grannell PK. NMR'diffraction'in solids? Journal of Physics C: solid state physics 1973;6(22):L422.
9. Stehling MK, Turner R, Mansfield P. Echo-planar imaging: magnetic resonance imaging in a fraction of a second. Science 1991;254(5028):43-50.
10. Rabi II, Ramsey N, Schwinger J. Use of rotating coordinates in magnetic resonance problems. Reviews of Modern Physics 1954;26(2):167.
11. Fick A. V. On liquid diffusion. The London, Edinburgh, and Dublin Philosophical Magazine and Journal of Science 1855;10(63):30-39.
12. Hahn EL. Spin echoes. Physical Review 1950;80(4):580.
13. Carr HY, Purcell EM. Effects of diffusion on free precession in nuclear magnetic resonance experiments. Physical Review 1954;94(3):630.
14. Torrey HC. Bloch equations with diffusion terms. Physical Review 1956;104(3):563.
15. Stejskal E, Tanner J. Spin diffusion measurements: spin echoes in the presence of a time‐dependent field gradient. The journal of chemical physics 1965;42(1):288-292.
16. Stepišnik J. Analysis of NMR self-diffusion measurements by a density matrix calculation. Physica B+ C 1981;104(3):350-364.
17. Stepišnik J. Time-dependent self-diffusion by NMR spin-echo. Physica B: Condensed Matter 1993;183(4):343-350.
18. Gore JC, Xu J, Colvin DC, Yankeelov TE, Parsons EC, Does MD. Characterization of tissue structure at varying length scales using temporal diffusion spectroscopy. NMR Biomed 2010;23(7):745-756.
19. Colvin DC, Yankeelov TE, Does MD, Yue Z, Quarles C, Gore JC. New insights into tumor microstructure using temporal diffusion spectroscopy. Cancer Res 2008;68(14):5941-5947.

20. Does MD, Parsons EC, Gore JC. Oscillating gradient measurements of water diffusion in normal and globally ischemic rat brain. Magn Reson Med 2003;49(2):206-215.
21. Colvin DC, Jourquin J, Xu J, Does MD, Estrada L, Gore JC. Effects of intracellular organelles on the apparent diffusion coefficient of water molecules in cultured human embryonic kidney cells. Magn Reson Med 2011;65(3):796-801.
22. Xu J, Does MD, Gore JC. Dependence of temporal diffusion spectra on microstructural properties of biological tissues. Magn Reson Imaging 2011;29(3):380-390.
23. Xu J, Li K, Smith RA, Waterton JC, Zhao P, Chen H, Does MD, Manning HC, Gore JC. Characterizing tumor response to chemotherapy at various length scales using temporal diffusion spectroscopy. PloS one 2012;7(7):e41714.
24. Xu J, Xie J, Jourquin J, Colvin DC, Does MD, Quaranta V, Gore JC. Influence of cell cycle phase on apparent diffusion coefficient in synchronized cells detected using temporal diffusion spectroscopy. Magnetic resonance in medicine : official journal of the Society of Magnetic Resonance in Medicine / Society of Magnetic Resonance in Medicine 2011;65(4):920-926.
25. Colvin DC, Loveless ME, Does MD, Yue Z, Yankeelov TE, Gore JC. Earlier detection of tumor treatment response using magnetic resonance diffusion imaging with oscillating gradients. Magnetic resonance imaging 2011;29(3):315-323.
26. Xu J, Harkins KD, Horch RA, Does MD, Gore JC. Dependence of temporal diffusion spectroscopy on axon size in white matter tracts of rat spinal cord. Proceedings of the 20th Annual Meeting of ISMRM, Melbourne, Australia, 2012; p0351.
27. Aggarwal M, Burnsed J, Martin LJ, Northington FJ, Zhang J. Imaging neurodegeneration in the mouse hippocampus after neonatal hypoxia-ischemia using oscillating gradient diffusion MRI. Magnetic resonance in medicine : official journal of the Society of Magnetic Resonance in Medicine / Society of Magnetic Resonance in Medicine 2014;72(3):829-840.
28. Aggarwal M, Jones MV, Calabresi PA, Mori S, Zhang J. Probing mouse brain microstructure using oscillating gradient diffusion MRI. Magn Reson Med 2012;67(1):98-109.
29. Portnoy S, Fichtner ND, Dziegielewski C, Stanisz MP, Stanisz GJ. In vitro detection of apoptosis using oscillating and pulsed gradient diffusion magnetic resonance imaging. NMR Biomed 2014;27(4):371-380.
30. Portnoy S, Flint JJ, Blackband SJ, Stanisz GJ. Oscillating and pulsed gradient diffusion magnetic resonance microscopy over an extended b-value range: implications for the characterization of tissue microstructure. Magnetic resonance in medicine : official journal of the Society of Magnetic Resonance in Medicine / Society of Magnetic Resonance in Medicine 2013;69(4):1131-1145.
31. Assaf Y, Blumenfeld-Katzir T, Yovel Y, Basser PJ. AxCaliber: a method for measuring axon diameter distribution from diffusion MRI. Magn Reson Med 2008;59(6):1347-1354.

32. Panagiotaki E, Walker-Samuel S, Siow B, Johnson SP, Rajkumar V, Pedley RB, Lythgoe MF, Alexander DC. Noninvasive quantification of solid tumor microstructure using VERDICT MRI. Cancer Res 2014;74(7):1902-1912.
33. Ong HH, Wehrli FW. Quantifying axon diameter and intra-cellular volume fraction in excised mouse spinal cord with q-space imaging. Neuroimage 2010;51(4):1360-1366.
34. Xu J, Li H, Harkins KD, Jiang X, Xie J, Kang H, Does MD, Gore JC. Mapping mean axon diameter and axonal volume fraction by MRI using temporal diffusion spectroscopy. NeuroImage 2014;103C:10-19.
35. Moseley ME, Kucharczyk J, Mintorovitch J, Cohen Y, Kurhanewicz J, Derugin N, Asgari H, Norman D. Diffusion-weighted MR imaging of acute stroke: correlation with T2-weighted and magnetic susceptibility-enhanced MR imaging in cats. AJNR Am J Neuroradiol 1990;11(3):423-429.
36. Padhani AR, Liu G, Koh DM, Chenevert TL, Thoeny HC, Takahara T, Dzik-Jurasz A, Ross BD, Van Cauteren M, Collins D, Hammoud DA, Rustin GJ, Taouli B, Choyke PL. Diffusion-weighted magnetic resonance imaging as a cancer biomarker: consensus and recommendations. Neoplasia 2009;11(2):102-125.
37. Patterson DM, Padhani AR, Collins DJ. Technology insight: water diffusion MRI--a potential new biomarker of response to cancer therapy. Nat Clin Pract Oncol 2008;5(4):220-233.
38. Zhao M, Pipe JG, Bonnett J, Evelhoch JL. Early detection of treatment response by diffusion-weighted 1H-NMR spectroscopy in a murine tumour in vivo. Br J Cancer 1996;73(1):61-64.
39. Squillaci E, Manenti G, Cova M, Di Roma M, Miano R, Palmieri G, Simonetti G. Correlation of diffusion-weighted MR imaging with cellularity of renal tumours. Anticancer Res 2004;24(6):4175-4179.
40. Sugahara T, Korogi Y, Kochi M, Ikushima I, Shigematu Y, Hirai T, Okuda T, Liang L, Ge Y, Komohara Y, Ushio Y, Takahashi M. Usefulness of diffusion-weighted MRI with echo-planar technique in the evaluation of cellularity in gliomas. J Magn Reson Imaging 1999;9(1):53-60.
41. Parsons EC, Jr., Does MD, Gore JC. Temporal diffusion spectroscopy: theory and implementation in restricted systems using oscillating gradients. Magn Reson Med 2006;55(1):75-84.
42. Wu D, Martin LJ, Northington FJ, Zhang J. Oscillating gradient diffusion MRI reveals unique microstructural information in normal and hypoxia-ischemia injured mouse brains. Magnetic resonance in medicine : official journal of the Society of Magnetic Resonance in Medicine / Society of Magnetic Resonance in Medicine 2014;72(5):1366-1374.
43. Baron CA, Beaulieu C. Oscillating gradient spin-echo (OGSE) diffusion tensor imaging of the human brain. Magn Reson Med 2014;72(3):726-736.
44. Kershaw J, Leuze C, Aoki I, Obata T, Kanno I, Ito H, Yamaguchi Y, Handa H. Systematic changes to the apparent diffusion tensor of in vivo rat brain measured with an oscillating-gradient spin-echo sequence. Neuroimage 2013;70:10-20.

45. Van AT, Holdsworth SJ, Bammer R. In vivo investigation of restricted diffusion in the human brain with optimized oscillating diffusion gradient encoding. Magn Reson Med 2014;71(1):83-94.
46. Stepisnik J. Analysis of Nmr Self-Diffusion Measurements by a Density-Matrix Calculation. Physica B & C 1981;104(3):350-364.
47. Xu J, Does MD, Gore JC. Quantitative characterization of tissue microstructure with temporal diffusion spectroscopy. Journal of magnetic resonance 2009;200(2):189-197.
48. Ianus A, Siow B, Drobnjak I, Zhang H, Alexander DC. Gaussian phase distribution approximations for oscillating gradient spin echo diffusion MRI. J Magn Reson 2013;227:25-34.
49. Li H, Gore JC, Xu J. Fast and robust measurement of microstructural dimensions using temporal diffusion spectroscopy. Journal of magnetic resonance 2014;242:4-9.
50. Douglass DC, McCall DW. Diffusion in paraffin hydrocarbons. J Phys Chem 1958;62(9):1102-1107.
51. Zielinski LJ, Sen PN. Effects of finite-width pulses in the pulsed-field gradient measurement of the diffusion coefficient in connected porous media. J Magn Reson 2003;165(1):153-161.
52. Stepisnik J. Time-Dependent Self-Diffusion by Nmr Spin-Echo. Physica B 1993;183(4):343-350.
53. Xu J, Does MD, Gore JC. Numerical study of water diffusion in biological tissues using an improved finite difference method. Phys Med Biol 2007;52(7):N111-126.
54. Ackerman JJ, Neil JJ. The use of MR-detectable reporter molecules and ions to evaluate diffusion in normal and ischemic brain. NMR Biomed 2010;23(7):725-733.
55. Shepherd TM, Thelwall PE, Stanisz GJ, Blackband SJ. Aldehyde fixative solutions alter the water relaxation and diffusion properties of nervous tissue. Magn Reson Med 2009;62(1):26-34.
56. Rohlmann A, Wolff J. Subcellular topography and plasticity of gap junction distribution on astrocytes. Gap junctions in the nervous system: Springer; 1996. p 175-192.
57. Bankir L, de Rouffignac C. Urinary concentrating ability: insights from comparative anatomy. Am J Physiol 1985;249(6 Pt 2):R643-666.
58. Samsonidze GG. Change in the size of the nucleus and body of cells in a rat's regenerating kidney. Biull Eksp Biol Med 1962;52:1072-1075.
59. Drochmans P, Wanson JC, Mosselmans R. Isolation and subfractionation on ficoll gradients of adult rat hepatocytes. Size, morphology, and biochemical characteristics of cell fractions. J Cell Biol 1975;66(1):1-22.
60. Tanner JE. Transient Diffusion in a System Partitioned by Permeable Barriers - Application to Nmr Measurements with a Pulsed Field Gradient. J Chem Phys 1978;69(4):1748-1754.
61. Watson C, Paxinos G, Puelles L. The mouse nervous system: Academic Press; 2012.

62. Zhao C, Teng EM, Summers RG, Jr., Ming GL, Gage FH. Distinct morphological stages of dentate granule neuron maturation in the adult mouse hippocampus. J Neurosci 2006;26(1):3-11.
63. Diaz-Cintra S, Yong A, Aguilar A, Bi X, Lynch G, Ribak CE. Ultrastructural analysis of hippocampal pyramidal neurons from apolipoprotein E-deficient mice treated with a cathepsin inhibitor. J Neurocytol 2004;33(1):37-48.
64. van Gelderen P, de Vleeschouwer MH, DesPres D, Pekar J, van Zijl PC, Moonen CT. Water diffusion and acute stroke. Magn Reson Med 1994;31(2):154-163.
65. Silva MD, Omae T, Helmer KG, Li F, Fisher M, Sotak CH. Separating changes in the intra- and extracellular water apparent diffusion coefficient following focal cerebral ischemia in the rat brain. Magn Reson Med 2002;48(5):826-837.
66. Harkins KD, Galons JP, Divijak JL, Trouard TP. Changes in intracellular water diffusion and energetic metabolism in response to ischemia in perfused C6 rat glioma cells. Magn Reson Med 2011;66(3):859-867.
67. Duong TQ, Ackerman JJ, Ying HS, Neil JJ. Evaluation of extra- and intracellular apparent diffusion in normal and globally ischemic rat brain via 19F NMR. Magn Reson Med 1998;40(1):1-13.
68. Waxman SG, Kocsis JD, Stys PK. The axon: structure, function, and pathophysiology: Oxford University Press; 1995.
69. Cory DG, Garroway AN. Measurement of translational displacement probabilities by NMR: an indicator of compartmentation. Magn Reson Med 1990;14(3):435-444.
70. Tanner JE. Intracellular Diffusion of Water. Arch Biochem Biophys 1983;224(2):416-428.
71. Szafer A, Zhong J, Gore JC. Theoretical model for water diffusion in tissues. Magn Reson Med 1995;33(5):697-712.
72. Xu J, Does MD, Gore JC. Sensitivity of MR Diffusion Measurements to Variations in Intracellular Structure: Effects of Nuclear Size. Magn Reson Med 2009;61(4):828-833.
73. Colvin DC, Jourquin J, Xu JZ, Does MD, Estrada L, Gore JC. Effects of Intracellular Organelles on the Apparent Diffusion Coefficient of Water Molecules in Cultured Human Embryonic Kidney Cells. Magn Reson Med 2011;65(3):796-801.
74. Beaulieu C. The basis of anisotropic water diffusion in the nervous system - a technical review. NMR Biomed 2002;15(7-8):435-455.
75. Day RE, Kitchen P, Owen DS, Bland C, Marshall L, Conner AC, Bill RM, Conner MT. Human aquaporins: Regulators of transcellular water flow. Bba-Gen Subjects 2014;1840(5):1492-1506.
76. Meier C, Dreher W, Leibfritz D. Diffusion in compartmental systems. I. A comparison of an analytical model with simulations. Magn Reson Med 2003;50(3):500-509.
77. Pfeuffer J, Flogel U, Dreher W, Leibfritz D. Restricted diffusion and exchange of intracellular water: theoretical modelling and diffusion time dependence of 1H NMR measurements on perfused glial cells. NMR Biomed 1998;11(1):19-31.

78. Pfeuffer J, Flogel U, Leibfritz D. Monitoring of cell volume and water exchange time in perfused cells by diffusion-weighted 1H NMR spectroscopy. NMR Biomed 1998;11(1):11-18.
79. Zhao L, Kroenke CD, Song J, Piwnica-Worms D, Ackerman JJ, Neil JJ. Intracellular water-specific MR of microbead-adherent cells: the HeLa cell intracellular water exchange lifetime. NMR Biomed 2008;21(2):159-164.
80. Thelwall PE, Grant SC, Stanisz GJ, Blackband SJ. Human erythrocyte ghosts: exploring the origins of multiexponential water diffusion in a model biological tissue with magnetic resonance. Magn Reson Med 2002;48(4):649-657.
81. Badaut J, Ashwal S, Adami A, Tone B, Recker R, Spagnoli D, Ternon B, Obenaus A. Brain water mobility decreases after astrocytic aquaporin-4 inhibition using RNA interference. J Cereb Blood Flow Metab 2011;31(3):819-831.
82. Meier C, Dreher W, Leibfritz D. Diffusion in compartmental systems. II. Diffusion-weighted measurements of rat brain tissue in vivo and postmortem at very large b-values. Magn Reson Med 2003;50(3):510-514.
83. Benveniste H, Hedlund LW, Johnson GA. Mechanism of detection of acute cerebral ischemia in rats by diffusion-weighted magnetic resonance microscopy. Stroke 1992;23(5):746-754.
84. Bailey C, Giles A, Czarnota GJ, Stanisz GJ. Detection of apoptotic cell death in vitro in the presence of Gd-DTPA-BMA. Magn Reson Med 2009;62(1):46-55.
85. Nilsson M, Latt J, van Westen D, Brockstedt S, Lasic S, Stahlberg F, Topgaard D. Noninvasive mapping of water diffusional exchange in the human brain using filter-exchange imaging. Magn Reson Med 2013;69(6):1573-1581.
86. Allen DG, Whitehead NP. Duchenne muscular dystrophy - What causes the increased membrane permeability in skeletal muscle? Int J Biochem Cell Biol 2011;43(3):290-294.
87. Hu J, Verkman AS. Increased migration and metastatic potential of tumor cells expressing aquaporin water channels. FASEB J 2006;20(11):1892-1894.
88. Jamur MC, Oliver C. Permeabilization of cell membranes. Methods Mol Biol 2010;588:63-66.
89. Seeman P, Cheng D, Iles GH. Structure of Membrane Holes in Osmotic and Saponin Hemolysis. J Cell Biol 1973;56(2):519-527.
90. Ash R, Barrer RM, Craven RJB. Sorption Kinetics and Time-Lag Theory .1. Constant Diffusion-Coefficient. J Chem Soc Farad T 2 1978;74:40-56.
91. Holz M, Heil SR, Sacco A. Temperature-dependent self-diffusion coefficients of water and six selected molecular liquids for calibration in accurate H-1 NMR PFG measurements. Phys Chem Chem Phys 2000;2(20):4740-4742.
92. Brahm J. Diffusional water permeability of human erythrocytes and their ghosts. J Gen Physiol 1982;79(5):791-819.
93. Ross BD, Moffat BA, Lawrence TS, Mukherji SK, Gebarski SS, Quint DJ, Johnson TD, Junck L, Robertson PL, Muraszko KM, Dong Q, Meyer CR, Bland PH, McConville P, Geng HR, Rehemtulla A, Chenevert TL. Evaluation of cancer therapy using diffusion magnetic resonance imaging. Mol Cancer Ther 2003;2(6):581-587.
94. Yoshikawa MI, Ohsumi S, Sugata S, Kataoka M, Takashima S, Mochizuki T, Ikura H, Imai Y. Relation between cancer cellularity and apparent diffusion

coefficient values using diffusion-weighted magnetic resonance imaging in breast cancer. Radiat Med 2008;26(4):222-226.
95. Aslund I, Nowacka A, Nilsson M, Topgaard D. Filter-exchange PGSE NMR determination of cell membrane permeability. J Magn Reson 2009;200(2):291-295.
96. Benga G, Pop VI, Popescu O, Borza V. On measuring the diffusional water permeability of human red blood cells and ghosts by nuclear magnetic resonance. J Biochem Biophys Methods 1990;21(2):87-102.
97. Quirk JD, Bretthorst GL, Duong TQ, Snyder AZ, Springer CS, Jr., Ackerman JJ, Neil JJ. Equilibrium water exchange between the intra- and extracellular spaces of mammalian brain. Magn Reson Med 2003;50(3):493-499.
98. Karger J. Determination of Diffusion in a 2 Phase System by Pulsed Field Gradients. Ann Phys-Berlin 1969;24(1-2):1-&.
99. Sigmund EE, Novikov DS, Sui D, Ukpebor O, Baete S, Babb JS, Liu K, Feiweier T, Kwon J, McGorty K, Bencardino J, Fieremans E. Time-dependent diffusion in skeletal muscle with the random permeable barrier model (RPBM): application to normal controls and chronic exertional compartment syndrome patients. NMR Biomed 2014;27(5):519-528.
100. Novikov DS, Fieremans E, Jensen JH, Helpern JA. Random walks with barriers. Nat Phys 2011;7(6):508-514.
101. Novikov DS, Jensen JH, Helpern JA, Fieremans E. Revealing mesoscopic structural universality with diffusion. Proc Natl Acad Sci U S A 2014;111(14):5088-5093.
102. Stanisz GJ, Szafer A, Wright GA, Henkelman RM. An analytical model of restricted diffusion in bovine optic nerve. Magn Reson Med 1997;37(1):103-111.
103. Mulkern RV, Gudbjartsson H, Westin CF, Zengingonul HP, Gartner W, Guttmann CR, Robertson RL, Kyriakos W, Schwartz R, Holtzman D, Jolesz FA, Maier SE. Multi-component apparent diffusion coefficients in human brain. NMR Biomed 1999;12(1):51-62.
104. Stanisz GJ. Diffusion MR in biological systems: Tissue compartments and exchange. Isr J Chem 2003;43(1-2):33-44.
105. Sukstanskii AL. Exact analytical results for ADC with oscillating diffusion sensitizing gradients. J Magn Reson 2013;234:135-140.
106. White NS, Dale AM. Distinct effects of nuclear volume fraction and cell diameter on high b-value diffusion MRI contrast in tumors. Magn Reson Med 2014;72(5):1435-1443.
107. Hursh JB. Conduction velocity and diameter of nerve fibers. American Journal of Physiology 1939;127:131-139.
108. Ritchie JM. On the relation between fibre diameter and conduction velocity in myelinated nerve fibres. Proc R Soc Lond B Biol Sci 1982;217(1206):29-35.
109. Callaghan PT, Coy A, Macgowan D, Packer KJ, Zelaya FO. Diffraction-Like Effects in Nmr Diffusion Studies of Fluids in Porous Solids. Nature 1991;351(6326):467-469.
110. Ong HH, Wright AC, Wehrli SL, Souza A, Schwartz ED, Hwang SN, Wehrli FW. Indirect measurement of regional axon diameter in excised mouse spinal cord

with q-space imaging: simulation and experimental studies. Neuroimage 2008;40(4):1619-1632.
111. Shemesh N, Ozarslan E, Basser PJ, Cohen Y. Measuring small compartmental dimensions with low-q angular double-PGSE NMR: The effect of experimental parameters on signal decay. J Magn Reson 2009;198(1):15-23.
112. Ozarslan E, Basser PJ. Microscopic anisotropy revealed by NMR double pulsed field gradient experiments with arbitrary timing parameters. The Journal of chemical physics 2008;128(15):154511.
113. Drobnjak I, Siow B, Alexander DC. Optimizing gradient waveforms for microstructure sensitivity in diffusion-weighted MR. J Magn Reson 2010;206(1):41-51.
114. Siow B, Drobnjak I, Chatterjee A, Lythgoe MF, Alexander DC. Estimation of pore size in a microstructure phantom using the optimised gradient waveform diffusion weighted NMR sequence. J Magn Reson 2012;214(1):51-60.
115. Alvarez GA, Shemesh N, Frydman L. Coherent dynamical recoupling of diffusion-driven decoherence in magnetic resonance. Physical review letters 2013;111(8):080404.
116. Shemesh N, Alvarez GA, Frydman L. Measuring small compartment dimensions by probing diffusion dynamics via Non-uniform Oscillating-Gradient Spin-Echo (NOGSE) NMR. Journal of magnetic resonance 2013;237:49-62.
117. Shemesh N, Ozarslan E, Basser PJ, Cohen Y. Detecting diffusion-diffraction patterns in size distribution phantoms using double-pulsed field gradient NMR: Theory and experiments. The Journal of chemical physics 2010;132(3):034703.
118. Callaghan PT. Pulsed-Gradient Spin-Echo Nmr for Planar, Cylindrical, and Spherical Pores under Conditions of Wall Relaxation. J Magn Reson Ser A 1995;113(1):53-59.
119. Neuman CH. Spin-Echo of Spins Diffusing in a Bounded Medium. Journal of Chemical Physics 1974;60(11):4508-4511.
120. Assaf Y, Freidlin RZ, Rohde GK, Basser PJ. New modeling and experimental framework to characterize hindered and restricted water diffusion in brain white matter. Magnet Reson Med 2004;52(5):965-978.
121. Schachter M, Does MD, Anderson AW, Gore JC. Measurements of restricted diffusion using an oscillating gradient spin-echo sequence. Journal of magnetic resonance 2000;147(2):232-237.
122. Baron CA, Beaulieu C. Oscillating Gradient Spin-Echo (OGSE) diffusion tensor imaging of the human brain. Magn Reson Med 2013.
123. Van AT, Holdsworth SJ, Bammer R. In vivo investigation of restricted diffusion in the human brain with optimized oscillating diffusion gradient encoding. Magnetic resonance in medicine : official journal of the Society of Magnetic Resonance in Medicine / Society of Magnetic Resonance in Medicine 2013.
124. Does MD, Parsons EC, Gore JC. Oscillating gradient measurements of water diffusion in normal and globally ischemic rat brain. Magnet Reson Med 2003;49(2):206-215.
125. Xu J, Does MD, Gore JC. Sensitivity of MR diffusion measurements to variations in intracellular structure: effects of nuclear size. Magnetic resonance in medicine :

official journal of the Society of Magnetic Resonance in Medicine / Society of Magnetic Resonance in Medicine 2009;61(4):828-833.
126. Aggarwal M, Burnsed J, Martin LJ, Northington FJ, Zhang J. Imaging neurodegeneration in the mouse hippocampus after neonatal hypoxia-ischemia using oscillating gradient diffusion MRI. Magn Reson Med 2013.
127. Ianus A, Siow B, Drobnjak I, Zhang H, Alexander DC. Gaussian phase distribution approximations for oscillating gradient spin echo diffusion MRI. J Magn Reson 2013;227:25-34.
128. Xu J, Does MD, Gore JC. Quantitative characterization of tissue microstructure with temporal diffusion spectroscopy. J Magn Reson 2009;200(2):189-197.
129. Waxman SG, Kocsis JD, Stys PK. The axon : structure, function and pathophysiology. New York ; Oxford: Oxford University Press; 1995. xv, 692 p., [692] of col. plates p.
130. Zielinski LJ, Sen PN. Effects of finite-width pulses in the pulsed-field gradient measurement of the diffusion coefficient in connected porous media. J Magn Reson 2003;165(1):153-161.
131. Frohlich AF, Jespersen SN, Ostergaard L, Kiselev VG. The effect of impermeable boundaries of arbitrary geometry on the apparent diffusion coefficient. J Magn Reson 2008;194(1):128-135.
132. Frohlich AF, Ostergaard L, Kiselev VG. Effect of impermeable boundaries on diffusion-attenuated MR signal. J Magn Reson 2006;179(2):223-233.
133. Douglass DC, McCall DW. Diffusion in Paraffin Hydrocarbons. The Journal of Physical Chemistry 1958;62(9):1102-1107.
134. Morozov D, Bar L, Sochen N, Cohen Y. Measuring small compartments with relatively weak gradients by angular double-pulsed-field-gradient NMR. Magnetic resonance imaging 2013;31(3):401-407.
135. Macomber J, Nico P, Nelson G. Internal diameter measurement of small bore capillary tubing. LCGC Application Notebook; June 2003. p 63.
136. Macomber J, Stasiak D. Strategies for reducing volumetric variance in precision small-bore flexible fused silica capillary pieces. LCGC Application Notebook; June 2007. p 73.
137. Siow B, Drobnjak I, Ianus A, N. CI, Lythgoe MF, Alexander DC. Axon radius estimation with oscillating gradient spin echo (OGSE) diffusion MRI. diffusion-fundamentalsorg 2013;18:1-6.
138. Stepisnik J. Validity limits of Gaussian approximation in cumulant expansion for diffusion attenuation of spin echo. Physica B 1999;270(1-2):110-117.
139. Sukstanskii AL, Yablonskiy DA. Gaussian approximation in the theory of MR signal formation in the presence of structure-specific magnetic field inhomogeneities. Effects of impermeable susceptibility inclusions. J Magn Reson 2004;167(1):56-67.
140. Hong XL, Dixon WT. Measuring Diffusion in Inhomogeneous Systems in Imaging Mode Using Antisymmetric Sensitizing Gradients. J Magn Reson 1992;99(3):561-570.
141. Sukstanskii AL. Exact analytical results for ADC with oscillating diffusion sensitizing gradients. J Magn Reson 2013;234:135-140.

142. Van Essen DC, Ugurbil K. The future of the human connectome. Neuroimage 2012;62(2):1299-1310.
143. Basser PJ, Mattiello J, LeBihan D. MR diffusion tensor spectroscopy and imaging. Biophysical journal 1994;66(1):259-267.
144. Wiegell MR, Larsson HB, Wedeen VJ. Fiber crossing in human brain depicted with diffusion tensor MR imaging. Radiology 2000;217(3):897-903.
145. Assaf Y, Basser PJ. Composite hindered and restricted model of diffusion (CHARMED) MR imaging of the human brain. Neuroimage 2005;27(1):48-58.
146. Kozlowski J, Konarzewski M, Gawelczyk AT. Cell size as a link between noncoding DNA and metabolic rate scaling. P Natl Acad Sci USA 2003;100(24):14080-14085.
147. Baserga R. Is cell size important? Cell cycle 2007;6(7):814-816.
148. Savage VM, Allen AP, Brown JH, Gillooly JF, Herman AB, Woodruff WH, West GB. Scaling of number, size, and metabolic rate of cells with body size in mammals. P Natl Acad Sci USA 2007;104(11):4718-4723.
149. Sun L, Sakurai S, Sano T, Hironaka M, Kawashima O, Nakajima T. High-grade neuroendocrine carcinoma of the lung: Comparative clinicopathological study of large cell neuroendocrine carcinoma and small cell lung carcinoma. Pathol Int 2009;59(8):522-529.
150. Brauer M. In vivo monitoring of apoptosis. Prog Neuro-Psychoph 2003;27(2):323-331.
151. Zink D, Fischer AH, Nickerson JA. Nuclear structure in cancer cells. Nat Rev Cancer 2004;4(9):677-687.
152. Hsu CY, Kurman RJ, Vang R, Wang TL, Baak J, Shih IM. Nuclear size distinguishes low- from high-grade ovarian serous carcinoma and, predicts outcome. Hum Pathol 2005;36(10):1049-1054.
153. Tobkes AI, Nord HJ. Liver-Biopsy - Review of Methodology and Complications. Digest Dis 1995;13(5):267-274.
154. Gauvain KM, McKinstry RC, Mukherjee P, Perry A, Neil JJ, Kaufman BA, Hayashi RJ. Evaluating pediatric brain tumor cellularity with diffusion-tensor imaging. Am J Roentgenol 2001;177(2):449-454.
155. Sugahara T, Korogi Y, Kochi M, Ikushima I, Shigematu Y, Hirai T, Okuda T, Liang LX, Ge YL, Komohara Y, Ushio Y, Takahashi M. Usefulness of diffusion-weighted MRI with echo-planar technique in the evaluation of cellularity in gliomas. Jmri-J Magn Reson Im 1999;9(1):53-60.
156. Szafer A, Zhong JH, Gore JC. Theoretical-Model for Water Diffusion in Tissues. Magn Reson Med 1995;33(5):697-712.
157. Torres AM, Michniewicz RJ, Chapman BE, Young GA, Kuchel PW. Characterisation of erythrocyte shapes and sizes by NMR diffusion-diffraction of water: correlations with electron micrographs. Magnetic resonance imaging 1998;16(4):423-434.
158. Mitra PP, Halperin BI. Effects of Finite Gradient-Pulse Widths in Pulsed-Field-Gradient Diffusion Measurements. J Magn Reson Ser A 1995;113(1):94-101.
159. Wang Y, Wang Q, Haldar JP, Yeh FC, Xie MQ, Sun P, Tu TW, Trinkaus K, Klein RS, Cross AH, Song SK. Quantification of increased cellularity during inflammatory demyelination. Brain : a journal of neurology 2011;134:3587-3598.

160. Assaf Y, Cohen Y. Assignment of the water slow-diffusing component in the central nervous system using q-space diffusion MRS: implications for fiber tract imaging. Magnetic resonance in medicine : official journal of the Society of Magnetic Resonance in Medicine / Society of Magnetic Resonance in Medicine 2000;43(2):191-199.
161. Barazany D, Basser PJ, Assaf Y. In vivo measurement of axon diameter distribution in the corpus callosum of rat brain. Brain : a journal of neurology 2009;132(Pt 5):1210-1220.
162. Alexander DC, Hubbard PL, Hall MG, Moore EA, Ptito M, Parker GJ, Dyrby TB. Orientationally invariant indices of axon diameter and density from diffusion MRI. NeuroImage 2010;52(4):1374-1389.
163. Dyrby TB, Sogaard LV, Hall MG, Ptito M, Alexander DC. Contrast and stability of the axon diameter index from microstructure imaging with diffusion MRI. Magnet Reson Med 2013;70(3):711-721.
164. Shemesh N, Ozarslan E, Basser PJ, Cohen Y. Accurate noninvasive measurement of cell size and compartment shape anisotropy in yeast cells using double-pulsed field gradient MR. Nmr Biomed 2012;25(2):236-246.
165. Gore JC, Xu JZ, Colvin DC, Yankeelov TE, Parsons EC, Does MD. Characterization of tissue structure at varying length scales using temporal diffusion spectroscopy. Nmr Biomed 2010;23(7):745-756.
166. Gross B, Kosfeld R. Anwendung der spin-echo-methode der messung der selbstdiffusion. Messtechnik 1969;77:171-177.
167. Marchadour C, Brouillet E, Hantraye P, Lebon V, Valette J. Anomalous diffusion of brain metabolites evidenced by diffusion-weighted magnetic resonance spectroscopy in vivo. Journal of cerebral blood flow and metabolism : official journal of the International Society of Cerebral Blood Flow and Metabolism 2012;32(12):2153-2160.
168. Colvin DC, Loveless ME, Does MD, Yue Z, Yankeelov TE, Gore JC. Earlier detection of tumor treatment response using magnetic resonance diffusion imaging with oscillating gradients. Magnetic resonance imaging 2011;29(3):315-323.
169. Siow B, Drobnjak I, Ianus A, Christie IN, Lythgoe MF, Alexander DC. Axon radius estimation with Oscillating Gradient Spin Echo (OGSE) Diffusion MRI. diffusion fundamentals 2013;18:1-6.
170. Assaf Y, Freidlin RZ, Rohde GK, Basser PJ. New modeling and experimental framework to characterize hindered and restricted water diffusion in brain white matter. Magnetic resonance in medicine : official journal of the Society of Magnetic Resonance in Medicine / Society of Magnetic Resonance in Medicine 2004;52(5):965-978.
171. Conover WJ. Practical nonparametric statistics. New York: Wiley; 1999. viii, 584 p. p.
172. Setsompop K, Kimmlingen R, Eberlein E, Witzel T, Cohen-Adad J, McNab JA, Keil B, Tisdall MD, Hoecht P, Dietz P, Cauley SF, Tountcheva V, Matschl V, Lenz VH, Heberlein K, Potthast A, Thein H, Van Horn J, Toga A, Schmitt F, Lehne D, Rosen BR, Wedeen V, Wald LL. Pushing the limits of in vivo diffusion MRI for the Human Connectome Project. NeuroImage 2013;80:220-233.

173. Van AT, Holdsworth SJ, Bammer R. In Vivo Investigation of Restricted Diffusion in the Human Brain with Optimized Oscillating Diffusion Gradient Encoding. Magnet Reson Med 2014;71(1):83-94.
174. Xu JZ, Xie JP, Jourquin J, Colvin DC, Does MD, Quaranta V, Gore JC. Influence of Cell Cycle Phase on Apparent Diffusion Coefficient in Synchronized Cells Detected Using Temporal Diffusion Spectroscopy. Magnet Reson Med 2011;65(4):920-926.
175. Quirk JD, Bretthorst GL, Duong TQ, Snyder AZ, Springer CS, Ackerman JJH, Neil JJ. Equilibrium water exchange between the intra- and extracellular spaces of mammalian brain. Magnet Reson Med 2003;50(3):493-499.
176. Karger J, Pfeifer, H., Heink, W. Principles and application of self-diffusion measurements by nuclear magnetic resonance. Advanced Magnetic Resonance 1988;12:1-89.